

# The impact of stratospheric ozone changes on downward wave coupling in the Southern Hemisphere

TIFFANY A. SHAW \*

*Lamont-Doherty Earth Observatory and Department of Applied Physics and Applied Mathematics,*

*Columbia University, New York, New York, USA*

JUDITH PERLWITZ †

*Cooperative Institute for Research in Environmental Sciences, University of Colorado, Boulder, Colorado, USA*

NILI HARNIK

*Department of Geophysics and Planetary Sciences, Tel Aviv University, Tel Aviv, Israel*

PAUL A. NEWMAN

*NASA Goddard Space Flight Center, Greenbelt, Maryland, USA*

STEVEN PAWSON

*Global Modeling and Assimilation Office, NASA Goddard Space Flight Center, Greenbelt, Maryland, USA.*

---

\* *Corresponding author address:* Dr. Tiffany A. Shaw, Lamont-Doherty Earth Observatory and Department of Applied Physics and Applied Mathematics, Columbia University, P.O. Box 1000, 61 Route 9W, Palisades, NY, 10964, E-mail: tas2163@columbia.edu

† Also at: NOAA/Earth System Research Laboratory, Physical Sciences Division, Boulder, Colorado

## ABSTRACT

The impact of stratospheric ozone changes on downward wave coupling between the stratosphere and troposphere in the Southern Hemisphere is investigated using a suite of Goddard Earth Observing System chemistry-climate model (GEOS CCM) simulations. Downward wave coupling occurs when planetary waves reflected in the stratosphere impact the troposphere. In reanalysis data, the climatological coupling occurs from September to December when the stratospheric basic state has a well defined high-latitude meridional waveguide in the lower stratosphere that is bounded above by a reflecting surface, called a bounded wave geometry. Reanalysis data suggests that downward wave coupling during November-December has increased during the last three decades.

The GEOS CCM simulation of the recent past captures the main features of downward wave coupling in the Southern Hemisphere. Consistent with the Modern Era Retrospective-analysis for Research and Application (MERRA) data set, wave coupling in the model maximizes during October-November when there is a bounded wave geometry configuration. However, the wave coupling in the model is stronger than in the MERRA data set, and starts earlier and ends later in the seasonal cycle. The late season bias is caused by a bias in the timing of the stratospheric polar vortex breakup.

Temporal changes in stratospheric ozone associated with past depletion and future recovery significantly impact downward wave coupling in the model. During the period of ozone depletion, the spring bounded wave geometry, which is favorable for downward wave coupling, extends into early summer, due to a delay in the vortex breakup date, and leads to increased downward wave coupling during November-December. During the period of ozone recovery, the stratospheric basic state during November-December shifts from a spring con-

figuration back to a summer configuration, where waves are trapped in the troposphere, and leads to a decrease in downward wave coupling. Model simulations with chlorine fixed at 1960 values and increasing greenhouse gases show no significant changes in downward wave coupling and confirm that the changes in downward wave coupling in the model are caused by ozone changes. The results reveal a new mechanism wherein stratospheric ozone changes can affect the tropospheric circulation.

# 1. Introduction

In a recent study Shaw et al. (2010) investigated the nature of downward wave coupling between the stratosphere and troposphere using the European Centre for Medium-Range Weather Forecasts 40-year Re-Analysis data set. Downward wave coupling occurs when planetary waves reflected in the stratosphere impact the troposphere and is distinct from zonal-mean coupling, which results from wave dissipation and its subsequent impact on the zonal-mean flow (Perlwitz and Harnik 2004). Shaw et al. (2010) showed that in the Southern Hemisphere downward wave coupling is the most important source of downward dynamical coupling between the stratosphere and troposphere on the intraseasonal time scale from September to December. The results were in agreement with Black and McDaniel (2007) who showed that the austral stratospheric final warming event involved significant zonally-asymmetric circulation changes in the troposphere. Shaw et al. (2010) showed that downward wave coupling occurs when the stratospheric basic state forms a bounded wave geometry involving a high-latitude meridional waveguide in the lower stratosphere bounded above by a vertical reflecting surface. The boundaries of the meridional waveguide and vertical reflecting surface represent barriers to meridional and vertical propagation, respectively. Shaw et al. (2010) noted that a high-latitude meridional waveguide is crucial for guiding upward propagating waves toward the vertical reflecting surface making it more likely that the wave will reflect and induce downward wave coupling.

The Southern Hemisphere has undergone significant climate changes during spring and summer in recent decades. In particular, a one-month delay in the breakup of the stratospheric vortex (Neff 1999; Waugh et al. 1999; Karpetchko et al. 2005; Black and McDaniel

2007) and a shift toward a positive southern annular mode index (Thompson and Solomon 2002) have been observed. These changes are most likely caused by stratospheric polar ozone depletion (e.g., Gillett and Thompson 2003; Perlwitz et al. 2008; Haigh and Roscoe 2009; McLandress et al. 2011; Polvani et al. 2011). In addition, Johanson and Fu (2007) noted a non-zonal contribution to trends in the Southern Hemisphere, which coincides with significant changes in planetary wave structure in both the troposphere and stratosphere (Neff et al. 2008; Hu and Fu 2009; Lin et al. 2009).

Using the Modern Era Retrospective-analysis for Research and Application data set, Harnik et al. (2010) show that the changes in the Southern Hemisphere from 1979 to 2009 coincide with an increase in downward wave coupling between the stratosphere and troposphere during spring and early summer. The increase in downward wave coupling is associated with an earlier onset of the spring wave geometry, which is favorable for wave reflection, and the persistence of this configuration into early summer. The extension into early summer is associated with the observed delay in vortex breakup since 1979, which has been attributed to ozone depletion (Langematz et al. 2003; Haigh and Roscoe 2009). However, the changes in downward wave coupling could not be directly attributed to ozone changes because individual forcings like sea-surface temperature variability, greenhouse gas changes, and ozone changes cannot be separated in reanalysis data.

Here we investigate the impact of ozone changes on downward wave coupling in the Southern Hemisphere using a suite of Goddard Earth Observing System Chemistry-Climate model simulations. Section 2 describes the reanalysis data, model simulations and diagnostics used in this study. In section 3 we evaluate the model's representation of downward wave coupling in the Southern Hemisphere. The impact of temporal ozone changes on downward

wave coupling is analyzed in detail in section 4. The results are summarized in section 5.

## 2. Data, model simulations and analysis approach

The reanalysis data used in this study are daily three-dimensional geopotential height fields, and monthly-mean zonal-mean zonal wind and temperature fields from the Modern Era Retrospective-analysis for Research and Application (MERRA) data set (Rienecker et al. 2008; Schubert et al. 2008) covering the period from 1979 to 2009. Shaw et al. (2010) analyzed downward wave coupling in the European Centre for Medium-Range Weather Forecasts (ECMWF) 40-year Re-Analysis (ERA-40) data set from 1979 to August 2002. They found that the diagnostics used to identify downward wave coupling in the Southern Hemisphere were robust among the MERRA and ERA-40 reanalysis data sets.

The model data used in this study are from a series of Goddard Earth Observing System Chemistry-Climate model (GEOS CCM) Version 1 simulations (Pawson et al. 2008). The chemistry and dynamics of the Southern Hemisphere stratosphere of this model version have been extensively evaluated (Stolarski et al. 2006; Eyring et al. 2006; Pawson et al. 2008; Waugh and Eyring 2008; Fogt et al. 2009). The model exhibits biases that are common to other CCMs including a delay in the breakup of the Southern Hemisphere stratospheric vortex. This delay is related to biases in the chemistry-dynamics interactions in the model. Compared to reanalysis, the stratospheric vortex in the Southern Hemisphere is too strong in early winter and too variable in late winter, there is a high initial bias in total ozone and a warm bias in lower stratospheric temperature when there is no ozone loss. Overall, Antarctic ozone loss and its associated cooling are overestimated in the model (Pawson et al. 2008).

Here we analyze five GEOS CCM simulations; three simulations of the recent past (P1, P2, P-CI1960) and two 21st century simulations (C21 and C21-CI1960). These five simulations were also analyzed by Perlwitz et al. (2008). The P1 (P2) simulations cover the period from 1950 (1951) to 2004. These reference simulations for the recent past are forced with observed changes in sea surface temperature (SST) and sea ice (HadISST, Rayner et al. 2003), greenhouse gas concentrations and halogens. The P2 simulation is initialized using output from the first year of the P1 simulation and thus the two simulations are different only in their initial conditions. Differences between the two simulations are used to characterize the internal variability in the GEOS model. The P-CI1960 simulation begins in 1960 and chlorine is held fixed at 1960 values while the model is forced with observed changes in SST and sea ice.

The C21 and C21-CI1960 simulations cover the period from 2001 to 2099. In both simulations the greenhouse gas concentrations follow the Intergovernmental Panel on Climate Change (IPCC) A1b scenario (medium, SRESA1B). In the C21 simulation, which is the reference simulation for the future, the halogens are prescribed according to the Ab scenario (World Meteorological Organization 2003) whereas in the C21-CI1960 simulation chlorine is held fixed at 1960 values. Both simulations are forced with SST and sea ice changes from a single IPCC Fourth Assessment Report SRESA1b simulation of the coupled atmosphere-ocean Community Climate System Model version 3.0.

The reference GEOS CCM simulations, which are forced with observed and future projected changes in halogens, simulate the initial development and deepening of the Antarctic ozone hole during the second part of the 20th century, with Antarctic ozone depletion maximizing from about 1990 to 2020, and ozone recovery during the 21st century (Perlwitz et al.

2008). The comparison between the 1960-fixed chlorine simulations (P-Cl1960, C21-Cl1960), in which no ozone hole evolves (e.g. Perlwitz et al. 2008; Waugh et al. 2009), and the reference simulations is used to assess the impact of ozone changes on downward wave coupling.

Downward wave coupling in the MERRA data set and the GEOS CCM is analyzed using the diagnostics of Shaw et al. (2010). In particular, the cross-correlation technique of Randel (1987) is used to isolate the upward and downward propagating planetary wave signals. The diagnostic considers two geopotential height Fourier coefficients of wavenumber  $k$  at two different latitudes and heights. It quantifies the correlation coherence and correlation phase of the two waves as a function of time lag. Statistically significant cross correlations for time lags when the stratosphere leads the troposphere indicate downward wave coupling. The statistical significance of the correlations is calculated by taking into account the autocorrelations of the time series (Lau and Chan 1983). We high-pass filter the wave signals to remove variability greater than a year in the data. Hence, the correlations clearly reflect intraseasonal variations in the stratospheric basic state, e.g. the evolution from an eastward zonal wind during winter and spring, which allows vertical wave propagation into the stratosphere, to westward zonal wind when waves are trapped in the troposphere during summer. As in Shaw et al. (2010) we focus on zonal wavenumber one (wave-1) and use a reference latitude band from 45 to 80°S and a reference level at 500 hPa. We choose to average wave-1 over a reference latitude band, rather than consider a specific latitude, to account for the change in position of the maximum heat flux throughout the seasonal cycle.

The downward wave coupling is subsequently related to the basic state zonal-mean zonal wind and temperature using the wave geometry diagnostic developed by Harnik and Lindzen (2001). This diagnostic separates the more commonly used index of refraction into vertical

and meridional wavenumber contributions. The wavenumbers are diagnosed from the solution to the wave equation associated with the conservation of potential vorticity in spherical coordinates linearized about a zonal-mean basic state. As for the squared index of refraction, waves propagate in the vertical (meridional) direction when  $m^2 > 0$  ( $l^2 > 0$ ), are evanescent when  $m^2 < 0$  ( $l^2 < 0$ ), and are reflected when  $m^2 = 0$  ( $l^2 = 0$ ). The wave geometry diagnostic is used to determine whether the stratospheric basic state allows wave propagation in the vertical and meridional directions. Shaw et al. (2010) showed that the seasonal evolution of the vertical Eliassen-Palm (EP) flux at 100 hPa integrated between 35 and 90°S and the meridional flux at 35° integrated between 100 and 10 hPa could be related to the seasonal evolution of the wave geometry. In particular, it was confirmed that there was an enhancement of meridional EP flux associated with propagation in the absence of a high-latitude meridional waveguide.

### 3. Model evaluation of downward wave-1 coupling

We begin our evaluation with an analysis of downward wave-1 coupling in the GEOS CCM in the Southern Hemisphere for two-month overlapping periods from August to December. We use model data from 1979 to 2004 since that is the period that overlaps with the MERRA data set. Figure 1 shows wave-1 cross correlations from 500 to 1 hPa for time lags between -10 and 10 days for the MERRA data set (left column) and the P1 and P2 simulations (middle and right columns, respectively). The reference level is 500 hPa and the wave-1 fields are averaged from 45 to 80°S. Since the reference level is in the troposphere, positive lags have the troposphere leading the stratosphere whereas negative lags have the stratosphere leading

the troposphere indicating upward and downward propagation respectively. Correlation coefficients larger than 0.18 are significant at the 99% level. The MERRA cross-correlations show significant downward wave coupling (significant correlations for negative lags) from September to December in agreement with ERA-40 (compare Fig. 1 left column to Fig. 1 in Shaw et al. 2010). The GEOS CCM cross-correlations capture the seasonal evolution of downward wave coupling with the maximum downward-wave correlations occurring during October-November. However, the P1 and P2 cross correlations show significant downward wave coupling over an extended period of time (August to January<sup>1</sup> in the model versus September to December in MERRA). Furthermore, the P1 cross correlations are stronger than those in MERRA. Since the P1 and P2 cross-correlations are in reasonable agreement we focus on the P1 simulation in the subsequent analysis.

Shaw et al. (2010) showed that the maximum downward wave correlations during October-November in the ERA-40 reanalysis data coincide with a stratospheric basic state that is favorable for planetary wave reflection and downward wave coupling. Figure 2 shows zonal-mean cross sections of the vertical wavenumber (top row) and meridional wavenumber (bottom row) during October-November for MERRA (left column) and the P1 simulation (right column). The shading indicates regions of wave evanescence. For the vertical wave number panels, the shading is bounded by the  $m = 0$  surface, which is called a vertical reflecting surface. For the meridional wave number panels, the meridional wave evanescence region is bounded by the  $l = 0$  surface (solid line) and the vertical reflecting surface is indicated by the dashed line. The contoured  $l$  region, which exists between  $l = 0$  surfaces, is called a meridional waveguide. The MERRA data set and the GEOS CCM wave geometries are

---

<sup>1</sup>Downward wave coupling in the GEOS CCM continues into December-January (not shown).

in very good agreement. They both have a high-latitude meridional waveguide in the lower stratosphere bounded above by a vertical reflecting surface. Shaw et al. (2010) called this configuration, which is favorable for wave reflection, a bounded wave geometry configuration. In this configuration, wave propagation is limited in the meridional direction by the high-latitude meridional waveguide, which exists from 50 to 70°S, and bounded in the vertical by the vertical reflecting surface, which spans the width of the waveguide above 10 hPa. The waveguide is crucial for guiding the upward propagating waves toward the vertical reflecting surface making it more likely that they will reflect and induce downward wave coupling.

The October-November bounded wave geometry coincides with a particular configuration of the stratospheric eastward jet. Figure 3 shows the zonal-mean zonal wind during October-November for MERRA (left panel) and the P1 simulation (right panel). The shaded regions represent regions of wave evanescence and are identical to the lower panels in Fig. 2. The stratospheric jet is tilted toward the pole with the jet maximum below 10 hPa and large negative vertical zonal wind shear above. The region of large negative vertical zonal wind shear coincides with the region of vertical wave evanescence from 10 to 1 hPa. The region of meridional wave evanescence between 40 to 50°S and 100 to 10 hPa coincide with regions of large negative meridional and vertical zonal wind shear. Both types of zonal wind shear contribute to a negative meridional potential vorticity gradient and thus a negative index of refraction, which is related to the vertical and meridional wave numbers according to (7) in Shaw et al. (2010).<sup>2</sup> Wave-1 can only propagate in the vertical direction in the unshaded region along the jet axis, which is bounded in the meridional and vertical directions by wave

---

<sup>2</sup>Vertical gradients in the Brunt-Vaisala frequency also contribute to the index of refraction [see (7) in Shaw et al. (2010)].

evanescence regions. Note that the critical surface, where the zonal-mean zonal wind equals zero (Charney and Drazin 1961), lies within the region of wave evanescence (i.e. within the shaded region).

In order to better understand the nature of downward wave coupling throughout the seasonal cycle we consider the seasonal evolution of the wave geometry. Figure 4 shows the seasonal cycle of the vertical wavenumber averaged between 50 and 70°S for MERRA (top left panel) and the P1 simulation (top right panel). The meridional averaging quantifies the vertical extent of the reflecting surface throughout the seasonal cycle. The contouring and shading are identical to the top panels of Fig. 2. The MERRA data set shows that there are two times during the seasonal cycle when there is a reflecting surface in the upper stratosphere: early winter (May to July) and spring to early summer (September to December) consistent with ERA-40 reanalysis (compare Fig. 4 top left panel to Fig. 3 top panel in Shaw et al. 2010). The early winter reflecting surface is not captured by P1, however there is a minimum in  $m$  at 3 hPa in April. The lack of a reflecting surface during early winter is most likely related to the biases in the model’s stratospheric jet during late fall/early winter (Pawson et al. 2008). The top panels of Fig. 4 reveal that the descent of the vertical reflecting surface during spring and early summer indicated by the thick solid line is faster in the reanalysis than in the model. This descent is associated with the lowering of the jet maximum and the region of large vertical zonal wind shear above (see Fig. 3) and also coincides with the descent of the critical surface for stationary planetary waves. The model bias in the descent of the vertical reflecting surface is most likely related to the delayed vortex breakup in the model. We calculated the average breakup day for the 1979 to 2004 period based on 10 hPa zonal wind values averaged between 50 and 70°S. The modeled stratospheric vortex

breaks up 20 days later than the vortex in reanalysis (December 8 in P1 versus November 18 in MERRA).

The bottom panels of Fig. 4 show the seasonal cycle of the meridional wavenumber averaged between 100 and 10 hPa for MERRA (bottom left panel) and the P1 simulation (bottom right panel). The vertical averaging quantifies the meridional extent of the lower stratospheric meridional waveguide throughout the seasonal cycle. Overlying the seasonal cycle of the meridional wavenumber is the seasonal cycle of the vertical wavenumber averaged from 10 to 1 hPa (shaded regions from top panels in Fig. 4), which when combined with the vertically averaged meridional wavenumber illustrates the boundedness of the wave geometry. The contouring and shading are identical to the lower panels of Fig. 2. In the MERRA data set, a high-latitude meridional waveguide forms from September to November in agreement with the ERA-40 reanalysis (compare Fig. 4 bottom left panel to Fig. 4 top panel in Shaw et al. 2010). In contrast, from March to August there is a very wide meridional waveguide, which allows meridional propagation into the subtropics and decreases the likelihood of downward wave coupling. The combined  $l$  and  $m$  seasonal cycle shows that the MERRA high-latitude meridional waveguide is bounded above by a vertical reflecting surface during October and November. In the P1 simulation the high-latitude meridional waveguide forms earlier (in August) and lasts longer (into December) as compared to reanalysis and is bounded in the vertical by a reflecting surface from October to December.

The seasonal cycle of the averaged vertical and meridional wavenumbers reveal biases in the GEOS CCM during August-September and November-December. In the case of November-December the biases are in both the vertical and meridional wavenumbers. Figure 5 shows zonal-mean cross sections of the vertical wavenumber (top row) and meridional

wavenumber (bottom row) during November-December for MERRA (left column) and the P1 simulation (right column). The contouring and shading are identical to Fig. 2. The vertical reflecting surface in P1 is higher than that in MERRA, which is related to the bias in the descent of the vertical reflecting surface seen in the seasonal cycle. In addition, the meridional wavenumber in P1 exhibits a pronounced evanescent region between 45 and 50°S, which forms a high-latitude meridional waveguide from 50 to 70°S. This high-latitude meridional waveguide during November -December seen in the seasonal cycle of the P1 simulation is not present in MERRA.

Overall, the GEOS CCM captures the main features of the seasonal cycle of downward wave coupling in the MERRA data set. The downward wave cross-correlations maximize in October-November when there is a bounded wave geometry similar to the MERRA data set. However, there are biases in the seasonal cycle of the wave geometry, which can be used to explain the biases in downward wave coupling. In particular, the large correlation values for positive and negative time lags in the P1 simulation during August-September are likely due to a combination of the high-latitude meridional waveguide during August and the larger variability of the stratospheric vortex during late winter/early spring. This larger vortex variability is a known model bias that has been linked to a bias in the amount of wave activity reaching the stratosphere (Pawson et al. 2008). A well-defined meridional waveguide acts to guide waves toward the stratosphere allowing more wave-induced deceleration of the stratospheric vortex. It means that a vertical reflecting surface, and therefore a bounded wave geometry, likely forms during late winter as part of the interannual variability of the vortex similar to the Northern Hemisphere (Perlwitz and Harnik 2003). Note that the lack of a vertical reflecting surface during early winter (May-June) in the GEOS CCM does not

lead to a bias in downward wave coupling. The stratospheric basic state during May-June does not involve a high-latitude meridional waveguide, which is a necessary condition for downward wave coupling (Shaw et al. 2010).

The P1 simulation biases during November-December can be related to biases in the vortex breakup date. Using the MERRA data set, Harnik et al. (2010) showed that the vortex breakup date represents the transition from a climatological spring wave geometry configuration, which is favorable for wave reflection and downward wave coupling, to a climatological summer configuration, which inhibits vertical wave propagation between the troposphere and stratosphere (see their Fig. 3b,c). Figure 6 shows the November (top row) and December (bottom row) zonal-mean zonal wind and wave evanescence regions for MERRA (left column) and P1 (right column). The mid-November vortex breakup date is apparent in the zonal wind and wave geometry. During November the configuration is a combination of pre- and post-vortex breakup wave geometries (Fig. 6 upper left panel). The stratospheric jet maximum and critical line are much lower than during October-November (see Fig. 3 left panel). This configuration allows limited upward and downward wave coupling. During December the MERRA zonal wind and wave geometry are clearly in a post-vortex breakup configuration (Fig. 6 lower left panel). The wave geometry exhibits a tropospheric cavity characterized by a tropospheric waveguide between 25 and 55°S and a vertical reflecting surface at 100 hPa (region denoted by the letter A in Fig. 6). This configuration inhibits vertical wave propagation above 100 hPa and thus inhibits upward and downward wave coupling. In contrast, the early-December vortex breakup date in P1 is consistent with a pre-vortex break up configuration during November (Fig. 6 upper right panel). The stratospheric jet maximum is around 30 hPa and critical line is just below 1 hPa. The wave evanescence re-

gion exhibits a bounded wave geometry (region denoted by the letter B in Fig. 6) similar to October-November (see Fig. 3 right panel), which allows significant upward and downward wave coupling. During December the configuration is a combination of pre- and post-vortex breakup wave geometries (Fig. 6 lower right panel) and resembles the MERRA configuration during November. The purely post-vortex breakup wave geometry does not occur in P1 until January (not shown). Overall, the biases in vortex breakup date in P1 extend the period during the seasonal cycle when the basic state wave geometry is favorable for downward wave coupling leading to the enhanced downward wave cross-correlations during November-December.

The impact of simulated ozone changes on the climatological downward wave coupling in the GEOS CCM can be assessed by comparing the reference P1 simulation to the P-C11960 sensitivity simulation. Figure 7 shows the cross correlations for the P1 simulation (left column, repeated from Fig. 1) and the P-C11960 (right column) sensitivity simulation. The main differences occur from October to December. In the P1 simulation downward wave coupling maximizes during October-November, as in reanalysis, whereas it maximizes during September-October in the P-C11960 simulation. The differences in the cross correlations between the two simulations are largest during November-December with the P-C11960 simulation having smaller correlations by 0.2 to 0.3 units for both positive and negative time lags (compare Fig. 7 bottom panels).

The differences in the cross correlations during November-December coincide with differences in wave geometry and reflect differences in the timing of vortex breakup in the two simulations. The average vortex breakup date in the P1 simulation is December 8 whereas it is November 13 in the P-C11960 simulation. Figure 8 shows the zonal-mean zonal wind dur-

ing November-December for the P1 (left panel) and the P-CI1960 simulations (right panel). The shaded regions represent regions of wave evanescence similar to Fig. 3. The November-December zonal wind and wave geometry in the P1 simulation exhibit a climatological spring configuration, which is pre-vortex breakup. The zonal wind is eastward up to 10 hPa and poleward of 50°S and the wave geometry involves a high-latitude meridional wave guide from 55 to 75°S, which is bounded above by a vertical reflecting surface at 10 hPa (indicated by the letter B in Fig. 8). In contrast, the P-CI1960 simulation zonal-mean zonal wind and wave geometry exhibit a climatological summer configuration, which is post-vortex breakup. The zonal-mean zonal wind is westward above 30 hPa. Furthermore, the wave geometry in the troposphere exhibits a cavity characterized by a tropospheric waveguide between 25 and 55°S and a vertical reflecting surface at 100 hPa (region denoted by the letter A in Fig. 8). This configuration inhibits vertical wave propagation above 100 hPa and thus inhibits upward and downward wave coupling. Note also that the position of the tropospheric jets in the two simulations is different. The tropospheric jet is shifted poleward in the P1 simulation relative to the P-CI1960 simulation, which enlarges the tropospheric wave guide in the P1 simulation and subsequently allows wave coupling to occur.

The comparison between the P1 and P-CI1960 simulations suggests that simulated ozone changes have a significant impact on upward and downward wave coupling during November-December due to their impact on the stratospheric basic state and consequently the vortex breakup date. Furthermore, it suggests that the late season bias in downward wave coupling in the GEOS model (as compared to MERRA) is associated with chemistry-dynamics interactions during late spring and early summer.

## 4. Impact of temporal changes in stratospheric ozone on downward wave coupling in the GEOS CCM

As discussed in the Introduction, Harnik et al. (2010) have shown that downward wave coupling in the Southern Hemisphere during November-December in the MERRA data set has increased significantly in recent decades and the increase is associated with change in the basic state and in particular the delay in vortex breakup since 1979. However, the changes in downward wave coupling could not be directly attributed to temporal ozone changes using the reanalysis data. In this section, we investigate the impact of temporal changes in ozone on downward wave coupling in the GEOS CCM. As described in section 2, the P1 and C21 GEOS simulations provide a near continuous simulation from 1950 to 2099 that includes ozone depletion until about year 2000 and ozone recovery during the 21st century. The P-CI1960 and C21-CI1960 simulations provide a near continuous simulation from 1960 to 2099 with chlorine fixed at 1960 values and temporal changes in greenhouse gases and SSTs. The comparison between the two sets of simulations will be used to assess the impact of temporal changes in ozone on downward wave coupling and separate it from the impact of greenhouse gas increases alone.

Figure 9 shows the time series of the wave-1 cross-correlations between 500 hPa and 30 hPa for wave-1 averaged from 45 to 80°S and for time lags between -10 and +10 days during November-December for the P1 (top left), C21 (top right), P-CI1960 (bottom left) and C21-CI1960 (bottom right) simulations. In the P1 and C21 simulations, the downward wave cross-correlations increase during the second half of the 20th century and then decrease during the 21st century. The temporal changes in downward wave coupling coincide with

an increase and subsequent decrease in upward wave propagation. The GEOS simulations with fixed chlorine at 1960 values (P-Cl1960 and C21-Cl1960) show no significant temporal changes in downward wave coupling after 1980. It is clear that the cause of the increase and subsequent decrease in downward wave coupling is the decrease and subsequent increase in stratospheric ozone. In particular, the maximum in downward wave coupling from 1990 to 2020 coincides with maximum ozone depletion.

In order to understand the temporal changes in downward wave coupling in the GEOS CCM simulations we consider temporal changes in the wave geometry. Figure 10 shows time series of the squared vertical wavenumber  $m^2$  averaged between 50 and 70°S and 30 to 10 hPa during November-December for all four GEOS simulations.<sup>3</sup> The averaging quantifies changes in the height of the climatological vertical reflecting surface during November-December (Fig. 8). The linear trend in the time series is shown as a thick straight line together with the absolute t-value indicating the statistical significance of the trend. An absolute value larger than 1.69 (2.26) indicates statistical significance at the 95% (99%) level. In the P1 simulation (Fig. 10, top left panel), covering the period from 1950 to 2004, there is a statistically significant positive trend in  $m^2$  from negative to positive values, which indicates that the region from 50 to 70°S and 30 to 10 hPa transitioned from a vertical wave evanescence region (with  $m^2 < 0$ ) to a vertical wave propagation region (with  $m^2 > 0$ ). This trend corresponds to a raising of the vertical reflecting surface to a level above 10 hPa. In the C21 simulation (Fig. 10, top right panel), covering the period from 2001 to 2099, there is a

---

<sup>3</sup>The time series of the squared wavenumbers are used to represent the transition from regions where waves can propagate ( $m^2 > 0$ ,  $l^2 > 0$ ) to regions where waves are evanescence ( $m^2 < 0$ ,  $l^2 < 0$ ), and visa versa.

statistically significant negative trend in  $m^2$  from positive to negative values, which indicates that the averaged region transitioned from a vertical wave propagation to a vertical wave evanescence region. This trend corresponds to a lowering of the height of the vertical reflecting surface to a level below 30 hPa. In contrast, the P-CI1960 and C21-CI1960 simulations (Fig. 10, bottom row) show no statistically significant change in  $m^2$  from 1960 to 2099.

Figure 11 shows the time series of the squared meridional wavenumber  $l^2$  averaged between 40 and 50°S and 100 to 10 hPa during November-December for the four GEOS simulations together with the linear trend line and the absolute t-value. The averaging quantifies changes in the width of the climatological meridional waveguide during November-December (Figs. 8). In particular, it quantifies the presence of a wave evanescence region in the lower stratosphere between 40 and 50°S and 100 to 10 hPa. In the P1 simulation (Fig. 11, top left panel) there is a statistically significant negative trend in  $l^2$  from positive to negative values, which indicates that the region from 40 to 50°S and 100 to 10 hPa transitioned from a meridional wave propagation region (with  $l^2 > 0$ ) to a meridional wave evanescence region (with  $l^2 < 0$ ) from 1950 to 2004. This trend corresponds to the formation of a high-latitude meridional waveguide between 50 and 70°. In the C21 simulation (Fig. 11, top right panel) there is a statistically significant positive trend from negative to positive values, which indicates that the averaged region transitioned from a meridional wave evanescence region to a meridional wave propagation region from 2001 to 2099. This trends correspond to a widening of the meridional waveguide. In contrast, both the P-CI1960 and the C21-CI1960 simulations (Fig. 11, bottom row) show a statistically significant increase in  $l^2$  from 1960 to 2099.

The trends in the squared wavenumbers suggest that the raising of the vertical reflecting

surface in the P1 simulation coincides with the formation of a high-latitude meridional waveguide on a multi-decadal time scale. Similarly, the lowering of the vertical reflecting surface in the C21 simulation coincides with the widening of the meridional waveguide. This relationship between the vertical and meridional wavenumbers is very robust and also occurs on the interannual time scale after the trend is removed. In particular, the correlation in the yearly de-trended time series of the squared vertical and meridional wavenumbers is -0.61 in the P1, -0.66 in C21, -0.62 in P-CI1960, and -0.38 in C21-CI1960.

The changes in the wave geometry can be linked to changes in the stratospheric basic state and in particular to changes in the vortex breakup date, which has consequences for the amplitude of wave-1 in the stratosphere. Figure 12 shows the time series of the vortex breakup day defined here as a change in sign of the zonal-mean zonal wind averaged between 50 and 70°S at 10 hPa for the four GEOS simulations together with the linear trend line and the absolute t-value. The vortex breakup day increases from 1950 to 2004 in the P1 simulation and then decreases from 2001 to 2099 in the C21 simulation (Fig. 12, top row). The positive trend in the vortex breakup date from 1979 to 2004 is consistent with the trends in the MERRA data set (see Fig. 5 in Harnik et al. 2010). There is no trend in the vortex breakup date in the P-CI1960 simulation and a small but significant increase in the vortex breakup date in the C21-CI1960 simulation (Fig. 12, bottom row). Figure 13 shows time series of the wave-1 amplitude averaged between 45 to 80°S at 5 hPa during November-December together with the linear trend line and the absolute t-value. The amplitude of wave-1 increases from 1950 to 2004 in the P1 simulation and decreases from 2001 to 2099 in the C21 simulation (Fig. 13, top row). Note that there are no significant trends in wave amplitude in the P-CI1960 and C21-CI1960 simulations (Fig. 13, bottom row).

The temporal evolution of the stratospheric basic state in the GEOS simulations for the December month is summarized in Figure 14, which shows the zonal-mean zonal wind and the wave evanescence regions from the December wave geometry for three decades: 1960 to 1970 (left column), 1994 to 2004 (middle column)<sup>4</sup> and 2089 to 2099 (right column) for the P1/C21 (top row) and P-Cl1960/C21-Cl1960 (bottom row) simulations. During the first decade, which is before ozone depletion, the average vortex breakup date occurs in late November for both the P1 and P-Cl1960 simulations. The corresponding December zonal-mean zonal wind and the wave geometry exhibit a climatological summer configuration; the zonal-mean zonal wind is westward above 30 hPa and the wave geometry exhibits a tropospheric cavity characterized by a tropospheric waveguide between 30 and 55°S bounded above by a vertical reflecting surface at 100 hPa (region denoted by the letter A in Fig. 14). This configuration inhibits vertical wave propagation above 100 hPa and thus inhibits upward and downward wave coupling. As a result, wave-1 amplitudes in the mid-latitude stratosphere are relatively small in both P1 and P-Cl1960 during this time (see Fig. 13 upper panels). During the second decade, which is at the peak of ozone depletion, the average vortex breakup date is during December in P1 and during November in P-Cl1960. The corresponding zonal-mean zonal wind and wave geometries are no longer similar. The zonal wind and wave geometry in the P1 simulation exhibit a climatological spring configuration; the zonal wind is eastward up to 10 hPa and poleward of 50°S and the wave geometry involves a high-latitude meridional wave guide from 55 to 75°S which is bounded above by a vertical reflecting surface at 10 hPa (region denoted by the letter B in Fig. 14). This configuration allows wave-1 propagation up

---

<sup>4</sup>The 1994 to 2004 basic state for P1 and P-Cl1960 are similar to the 2001-2010 basic states from C21 and C21-Cl1960, respectively.

to 10 hPa (see unshaded region south of 55°S) and is therefore also favorable for downward wave coupling. In contrast, the zonal wind and wave geometry in the P-C11960 simulation has not changed substantially; it still exhibits a climatological summer configuration with westward zonal winds above 30 hPa and a tropospheric cavity type wave geometry (region denoted by the letter A in Fig. 14) that inhibits upward and downward wave coupling. Wave-1 amplitudes in the stratosphere differ strongly between the two simulations during this time; the wave-1 amplitude in the P1 simulation is much stronger than in the P-C11960 simulation. Finally, during the third decade which is after ozone recovery, the average vortex breakup date for both C21 and C21-C11960 is in November. The corresponding post-vortex break up zonal-mean zonal wind and wave geometries in December once again exhibit a climatological summer configuration. In both simulations, the zonal wind and wave geometries are very similar to the 1960 to 1970 average and the wave-1 amplitudes are both relatively weak.

The combined past and future GEOS CCM simulations forced with and without changes in chlorine loading clearly demonstrate that temporal changes in ozone cause significant temporal changes in downward wave coupling between the stratosphere and troposphere during late spring and early summer. In particular, during the period of ozone depletion downward wave coupling during November-December increases while during ozone recovery it decreases. These changes are caused by temporal changes in the stratospheric basic state attributed to the simulated ozone changes. In the simulations with fixed chlorine loading and increasing greenhouse gases there is no significant change in downward wave coupling. Thus, the impact of increasing greenhouse gases on the stratospheric basic state and downward wave coupling is very small compared to the impact of ozone changes in the Southern Hemisphere.

## 5. Summary and discussion

We have examined the impact of stratospheric ozone changes on downward wave-1 coupling in the Southern Hemisphere using a suite of GEOS CCM simulations. Downward wave coupling was quantified using the cross-spectral correlation diagnostic of Randel (1987) and the wave geometry diagnostic of Harnik and Lindzen (2001).

The GEOS CCM captures the main features of downward wave coupling in the Southern Hemisphere from 1979 to 2004. Consistent with the MERRA data set, downward wave coupling in the model maximizes during October-November when the stratospheric basic state exhibits a bounded wave geometry associated with a high-latitude meridional waveguide in the lower stratosphere bounded above by a vertical reflecting surface in the mid-to-upper stratosphere. The vertical reflecting surface in the stratosphere is associated with strong negative vertical zonal wind shear above the vortex maximum. The high-latitude meridional wave guide is associated with large negative meridional and vertical zonal wind shear in the lower stratosphere between 40 and 50°S. The model, however, exhibits a bias in its seasonal cycle of downward wave coupling. In the reference GEOS CCM simulation forced by observed changes in greenhouse gases, halogens, SSTs and sea ice, downward wave coupling begins in August and ends in January whereas it occurs from September to December in both the ERA-40 (Shaw et al. 2010) and the MERRA data sets. A comparison of the reference simulation with a sensitivity simulation with chlorine fixed at 1960 values revealed that the model's enhanced downward wave coupling from November to January was due to biases in chemistry-dynamics interactions, which leads to a delayed vortex breakup and is a known bias of the GEOS CCM (Pawson et al. 2008). The delay in vortex breakup date extends the

spring wave geometry configuration, which is favorable for wave reflection and downward wave coupling, from late spring to early summer causing the increase of both upward and downward wave coupling.

The impact of temporal changes in ozone on downward wave coupling was investigated using GEOS CCM simulations of the recent past and 21st century with and without chlorine changes. The simulations reveal that downward wave coupling during November-December maximizes during the period of maximum Antarctic ozone depletion. During the periods of ozone depletion and recovery downward wave coupling increases and decreases, respectively. The changes in wave coupling coincide with changes in the stratospheric basic state and wave geometry. During the period of ozone depletion the spring wave geometry configuration extends into early summer, due to a delay in vortex breakup, and leads to increased downward wave coupling during November-December. During the period of ozone recovery the stratospheric basic state during November-December shifts from a spring configuration back to a summer configuration, where waves are trapped in the troposphere, which leads to a decrease in downward wave coupling. The GEOS simulations with fixed chlorine loading and increasing greenhouse gases have no significant change in downward wave coupling. The weak coupling in the fixed chlorine simulations coincides with weak trends in the vortex breakup date and wave geometry. During November-December, greenhouse gas changes mainly impacts the tropospheric jet and in particular the position of the zero wind line between 40 to 60°S, which does not strongly affect downward wave coupling. The results confirm that the changes in wave coupling during November-December are caused by ozone changes and not by changes in greenhouse gases.

The increase in downward wave coupling during the period of ozone depletion in the

GEOS CCM is consistent with the increase in downward wave coupling during November-December from 1979 to 2009 in the MERRA data set (Harnik et al. 2010). Harnik et al. (2010) suggested that ozone depletion was the likely cause of the changes. Our results clearly attribute the change in downward wave coupling in the GEOS model to ozone changes and suggest that as ozone recovers during the 21st century downward wave coupling during November-December is expected to decrease.

In a recent study, McLandress et al. (2010) used a series of Canadian Middle Atmosphere Model (CMAM) simulations with and without chlorine changes to investigate the separate impacts of ozone changes and greenhouse gas increases on the Southern Hemisphere stratosphere. The vortex breakup trends in the GEOS CCM simulation with and without chlorine changes are consistent with those found for the CMAM. McLandress et al. (2010) also noted trends in the summer Eliassen-Palm flux divergence, which are consistent with the GEOS CCM wave amplitude trends and the decadal change in the wave geometry. However, their interpretation of the changes is focused on changes in the critical line and wave dissipation. Here we have stressed changes in the wave geometry also lead to changes in downward wave coupling.

Overall, most of the previous studies on the impact of stratospheric ozone depletion on the tropospheric circulation have focused on changes in the zonal-mean circulation, i.e. changes in the Southern Hemisphere annular mode, which result from changes in zonal-mean downward coupling between the stratosphere and troposphere (Thompson and Solomon 2002; Son et al. 2010). Our results show that stratospheric ozone changes also cause changes in downward wave coupling between the stratosphere and troposphere. The increase in wave coupling will directly impact stationary waves in the troposphere. As mentioned in the

Introduction, non-zonal trends in the Southern Hemisphere have been observed since 1979 (Johanson and Fu 2007; Neff et al. 2008; Hu and Fu 2009; Lin et al. 2009). Understanding how an increase in downward wave coupling affects the tropospheric circulation and to what extent changes in downward wave coupling can explain non-zonal trends in the Southern Hemisphere is work in progress.

Our results reveal that a delayed vortex breakup bias in a CCM not only extends the period of upward wave propagation from the troposphere to the stratosphere, it also affects the tropospheric circulation due to exaggerated downward wave coupling. Climate models must accurately represent the stratospheric basic state wave geometry, planetary wave propagation and ozone changes in order to properly capture the impact of stratospheric ozone changes on tropospheric climate. The evaluation of the GEOS CCM showed that cross-spectral correlation and wave geometry diagnostics are the appropriate tools for diagnosing downward wave coupling in atmospheric general circulation models.

*Acknowledgments.*

We thank NASA's Global Modeling and Assimilation Office for providing the MERRA data set. This work was supported by the NASA Modeling and Analysis Program and used high-end computational resources provided by NASA's Columbia Project. TASs contribution was supported by the National Sciences and Engineering Research Council of Canada through a Post Doctoral Fellowship. NHs contribution was funded by grant 1370/08 from the Israeli Science Foundation. The authors are grateful to two anonymous reviewers for their helpful comments.

## REFERENCES

- Black, R. X. and B. A. McDaniel, 2007: Interannual variability in the southern hemisphere circulation organized by stratospheric final warming events. *J. Atmos. Sci.*, **64**, 2968–2974.
- Charney, J. G. and P. G. Drazin, 1961: Propagation of planetary disturbances from the lower into the upper atmosphere. *J. Geophys. Res.*, **66**, 83–109.
- Eyring, V., et al., 2006: Assessment of temperature, trace species, and ozone in chemistry-climate model simulations of the recent past. *J. Geophys. Res.*, **111**, 10.1029/2006JD0073272.
- Fogt, R. L., J. Perlwitz, S. Pawson, and M. A. Olsen, 2009: Intra-annual relationships between polar ozone and the SAM. *Geophys. Res. Lett.*, **36**, 10.1029/2008GL036627.
- Gillett, N. P. and D. W. J. Thompson, 2003: Simulation of recent southern hemisphere climate change. *Science*, **302**, 273–275.
- Haigh, J. D. and H. K. Roscoe, 2009: The final warming date of the antarctic polar vortex and influences on its interannual variability. *J. Climate*, **22**, 5809–5819.
- Harnik, N. and R. S. Lindzen, 2001: The effect of reflecting surfaces on the vertical structure and variability of stratospheric planetary waves. *J. Atmos. Sci.*, **58**, 2872–2894.
- Harnik, N., J. Perlwitz, and T. A. Shaw, 2010: Observed decadal changes in downward

- wave coupling between the stratosphere and troposphere in the southern hemisphere. *J. Climate*, submitted.
- Hu, Y. and Q. Fu, 2009: Stratospheric warming in southern hemisphere high latitudes since 1979. *Atmos. Chem. Phys.*, 4329–4340.
- Johanson, C. M. and Q. Fu, 2007: Antarctic atmospheric temperature trend patterns from satellite observations. *Gephys. Res. Lett.*, **34**, 10.1029/2006GL029108.
- Karpetchko, A., E. Kyrö, and B. M. Knudsen, 2005: Arctic and antarctic polar vortices 19572002 as seen from the ERA-40 reanalyses. *J. Geophys. Res.*, **110**, doi:10.1029/2005JD006113.
- Langematz, U., M. Kunze, K. Krger, K. Labitzke, and G. L. Roff, 2003: Thermal and dynamical changes of the stratosphere since 1979 and their link to ozone and CO2 changes. *J. Geophys. Res.*, **108**, doi:10.1029/2002JD002069.
- Lau, K. M. and P. H. Chan, 1983: Short-term climate variability and atmospheric teleconnections from satellite-observed outgoing longwave radiation. Part II: Lagged correlations. *J. Atmos. Sci.*, **40**, 2751–2767.
- Lin, P., Q. Fu, S. Solomon, and J. M. Wallace, 2009: Temperature trend patterns in the southern hemisphere high latitudes: Novel indicators of stratospheric change. *J. Climate*, **22**, 6325–6341.
- McLandress, C., A. I. Jonsson, D. A. Plummer, M. C. Reader, J. F. Scinocca, and T. G. Shepherd, 2010: Separating the dynamical effects of climate change and ozone depletion. part i: Southern hemisphere stratosphere. *J. Climate*, **23**, 5002–5020.

- McLandress, C., T. G. Shepherd, J. F. Scinocca, D. A. Plummer, M. Sigmond, A. I. Jonsson, and M. C. Reader, 2011: Separating the dynamical effects of climate change and ozone depletion: Part 2. southern hemisphere troposphere. *J. Climate*, in press.
- Neff, W., 1999: Decadal time scale trends and variability in the tropospheric circulation over the south pole. *J. Geophys. Res.*, **104**, 27 217–27 251.
- Neff, W., J. Perlwitz, and M. Hoerling, 2008: Observational evidence for asymmetric changes in tropospheric heights over Antarctica on decadal time scales. *Geophys. Res. Lett.*, **35**, doi:10.1029/2008GL035074.
- Pawson, S., R. S. Stolarski, A. R. Douglass, P. A. Newman, S. R. Frith, and M. K. Gupta, 2008: Goddard Earth Observing System chemistry-climate model simulations of stratospheric ozone-temperature coupling between 1950 and 2005. *J. Geophys. Res.*, **35**, doi:10.1029/2007JD009511.
- Perlwitz, J. and N. Harnik, 2003: Observational evidence of a stratospheric influence on the troposphere by planetary wave reflection. *J. Climate*, **16**, 3011–3026.
- Perlwitz, J. and N. Harnik, 2004: Downward coupling between the stratosphere and troposphere: The relative roles of wave and zonal mean processes. *J. Climate*, **17**, 4902–4909.
- Perlwitz, J., S. Pawson, R. Fogt, J. E. Nielsen, and W. Neff, 2008: The impact of stratospheric ozone hole recovery on antarctic climate. *Geophys. Res. Lett.*, **35**, doi:10.1029/2008GL033317.
- Polvani, L. M., D. Waugh, G. Correa, and S.-W. Son, 2011: Stratospheric ozone deple-

- tion: the main driver of 20th century atmospheric circulation changes in the southern hemisphere. *J. Climate*, in press.
- Randel, W. J., 1987: A study of planetary waves in the southern winter troposphere and stratosphere. Part I: Wave structure and vertical propagation. *J. Atmos. Sci.*, **44**, 917–935.
- Rayner, N. A., D. E. Parker, E. B. Horton, C. K. Folland, L. V. Alexander, D. P. Rowell, E. C. Kent, and A. Kaplan, 2003: Global analyses of sea surface temperature, sea ice, and night marine air temperature since the late nineteenth century. *J. Geophys. Res.*, **108**, doi:10.1029/2002JD002670.
- Rienecker, M. M., et al., 2008: The geos-5 data assimilation system - documentation of versions 5.0.1, 5.1.0, and 5.2.0. *Technical Report Series on Global Modeling and Data Assimilation*, **27**.
- Schubert, S., et al., 2008: Assimilating earth system observations at NASA: MERRA and beyond. Third WCRP International Conference on Reanalysis, Tokyo, Japan, [http://wcrp.ipsl.jussieu.fr/Workshops/Reanalysis2008/Documents/V1-104\\_ea.pdf](http://wcrp.ipsl.jussieu.fr/Workshops/Reanalysis2008/Documents/V1-104_ea.pdf).
- Shaw, T. A., J. Perlwitz, and N. Harnik, 2010: Downward wave coupling between the stratosphere and troposphere: The importance of meridional wave guiding and comparison with zonal-mean coupling. *J. Climate*, **23**, 6365–6381.
- Son, S.-W., E. P. Gerber, J. Perlwitz, L. M. Polvani, N. Gillett, K.-H. Seo, and S. co authors, 2010: The impact of stratospheric ozone on southern hemisphere circulation change: A multimodel assessment. *J. Geophys. Res.*, in press.

- Stolarski, R. S., A. R. Douglass, M. Gupta, P. A. Newman, S. Pawson, M. R. Schoeberl, and J. E. Nielsen, 2006: An ozone increase in the Antarctic summer stratosphere: A dynamical response to the ozone hole. *Geophys. Res. Lett.*, **33**, doi:10.1029/2006GL026820.
- Thompson, D. W. J. and S. Solomon, 2002: Interpretation of recent southern hemisphere climate change. *Science*, **296**, 895–899.
- Waugh, D. W. and V. Eyring, 2008: Quantitative performance metrics for stratospheric-resolving chemistry-climate models. *Atmos. Chem. Phys.*, **8**, 5699–5731.
- Waugh, D. W., L. Oman, S. R. Kawa, R. S. Stolarski, S. Pawson, A. R. Douglass, P. A. Newman, and J. E. Nielsen, 2009: Impacts of climate change on stratospheric ozone recovery. *Geophys. Res. Lett.*, **36**, doi:10.1029/2008GL036223.
- Waugh, D. W., W. J. Randel, S. Pawson, P. A. Newman, and E. R. Nash, 1999: Persistence of the lower stratospheric polar vortices. *J. Geophys. Res.*, **104**, 27 191–27 201.
- World Meteorological Organization, 2003: Scientific assessment of ozone depletion: 2002, Rep. 47. Global Ozone Res. and Monit. Proj.

## List of Figures

- 1 Vertical-time lag section of the correlation coherence for wave-1 averaged from 45 to 80°S at 500 hPa with vertical levels between 500 and 1 hPa for two-month overlapping periods from August-September to November-December 1979 to 2004 and for time lags between -10 and 10 days. For negative time lags the stratosphere is leading the troposphere. The cross-correlations are shown for the MERRA data set (left column) and the P1 (middle column) and P2 (right column) GEOS CCM simulations. Only correlations which are statistically significant at the 99% levels are contoured and the contour interval is 0.1. 37
- 2 Zonal-mean cross sections of the climatological vertical (top row) and meridional (bottom row) wavenumbers during October-November from 1979 to 2004 for the MERRA data set (left column) and the P1 GEOS CCM simulation (right column). For the vertical wavenumber the contours (units  $10^{-5} \text{ m}^{-1}$ ) are shown at 0.01 (thick line); 2, 4 (dashed line); 6-30 in jumps of 3 (thin lines) and the shading indicates regions of wave evanescence ( $m^2 < 0$ ). For the meridional wavenumber, the contour interval is  $1 \text{ rad}^{-1}$ , the thick line represents the 0.01 contour and the dashed line indicates the position of the vertical reflecting surface. Finally, the shading indicates regions of wave evanescence in the meridional ( $l^2 < 0$  bounded by solid line) and vertical ( $m^2 < 0$  bounded by dashed line) directions. 38

- 3 Zonal-mean zonal wind during October-November from 1979 to 2004 for the MERRA data set (left panel) and the P1 GEOS CCM simulation (right panel). Contour interval is  $5 \text{ ms}^{-1}$  and negative contours are dashed. The thick line indicates the zero zonal-wind line and the shading represents regions of wave evanescence and is identical to the shaded regions in the lower panels of Fig. 2. 39
- 4 The climatological seasonal cycle of the vertical (top row) and meridional (bottom row) wavenumbers averaged between  $50$  and  $70^\circ\text{S}$  and  $100$  and  $10$  hPa, respectively from 1979 to 2004 for the MERRA data set (left column) and the P1 GEOS CCM simulation (right column). Contouring and shading as in Fig. 2. The thick solid lines in the upper panels show the approximate linear descent rate. Overlying the climatological seasonal cycle of the meridional wavenumber is the seasonal cycle of the vertical wavenumber averaged between  $3$  and  $1$  hPa. 40
- 5 Zonal-mean cross sections of the vertical (top row) and meridional (bottom row) wavenumbers during November-December from 1979 to 2004 for the MERRA data set (left column) and the P1 GEOS CCM simulation (right column). Contouring and shading as in Fig. 2. 41

- 6 Zonal-mean zonal wind during November (top row) and December (bottom row) from 1979 to 2004 for the MERRA data set (left column) and the P1 GEOS CCM simulation (right column). Contour interval is  $5 \text{ ms}^{-1}$  and negative contours are dashed. The thick line indicates the zero zonal-wind line and the shading represents regions of vertical and meridional wave evanescence. Letters A and B indicated regions discussed in the text. 42
- 7 Vertical-time lag section of the correlation coherence for wave-1 averaged from  $45$  to  $80^\circ\text{S}$  at  $500 \text{ hPa}$  with vertical levels between  $500$  and  $1 \text{ hPa}$  for two-month overlapping periods from August-September to November-December 1979 to 2004 and for time lags between  $-10$  and  $10$  days. The cross-correlations are shown for the P1 (left column, repeated from Fig. 1) and the P-CI1960 (right column) GEOS CCM simulations. Contours and significance as in Fig. 1. 43
- 8 Zonal-mean zonal wind during November-December from 1979 to 2004 for the P1 (left panel) and the P-CI1960 (right panel) GEOS CCM simulations. Contours and shading as in Fig. 3. Letters A and B indicated regions discussed in the text. 44
- 9 Time series of the wave-1 cross-coherence correlations between  $30 \text{ hPa}$  and  $500 \text{ hPa}$  for wave-1 averaged from  $45$  to  $80^\circ\text{S}$  (solid lines) and for time lags between  $-10$  and  $10$  days during November-December. The correlation time series are shown for the P1 (top left), C21 (top right), P-CI1960 (bottom left) and C21-CI1960 (bottom right) GEOS CCM simulations. The cross correlations were determined based on 15-year overlapping periods. 45

- 10 Time series of the squared vertical wavenumber averaged between 50 and 70°S and 30 to 10 hPa for the P1 (top left), C21 (top right), P-CI1960 (bottom left) and C21-CI1960 (bottom right) GEOS CCM simulations. The thick solid line shows the linear regression and the associated t-value is shown at the bottom of each plot. 46
- 11 Time series of the squared meridional wavenumber averaged between 40 and 50°S and 100 to 10 hPa for the P1 (top left), C21 (top right), P-CI1960 (bottom left) and C21-CI1960 (bottom right) GEOS CCM simulations. The thick solid straight line shows the linear regression and the associated t-value is shown at the bottom of each plot. 47
- 12 Time series of the vortex breakup day, defined as the first day when the zonal-mean zonal wind averaged between 50 and 70°S at 10 hPa is negative, for the P1 (top left), C21 (top right), P-CI1960 (bottom left) and C21-CI1960 (bottom right) GEOS CCM simulations. The thick solid line shows the linear regression and the associated t-value is shown at the bottom of each plot. 48
- 13 Time series of wave-1 amplitude averaged between 45 and 80°S at 5 hPa for the P1 (top left), C21 (top right), P-CI1960 (bottom left) and C21-CI1960 (bottom right) GEOS CCM simulations. The thick solid line shows the linear regression and the associated t-value is also shown. 49

14 Zonal-mean zonal wind and wave evanescence regions from the wave geometry (indicated by shading) from 1960 to 1970 (left column), 1994 to 2004 (middle column), and 2089 to 2099 (right column) during December for the P1 (top two left panels), C21 (top right panel), P-CI1960 (bottom two left panels) and C21-CI1960 (bottom right panel) GEOS CCM simulations. Contours as in Fig. 3. Letters A and B indicated regions discussed in the text.

50

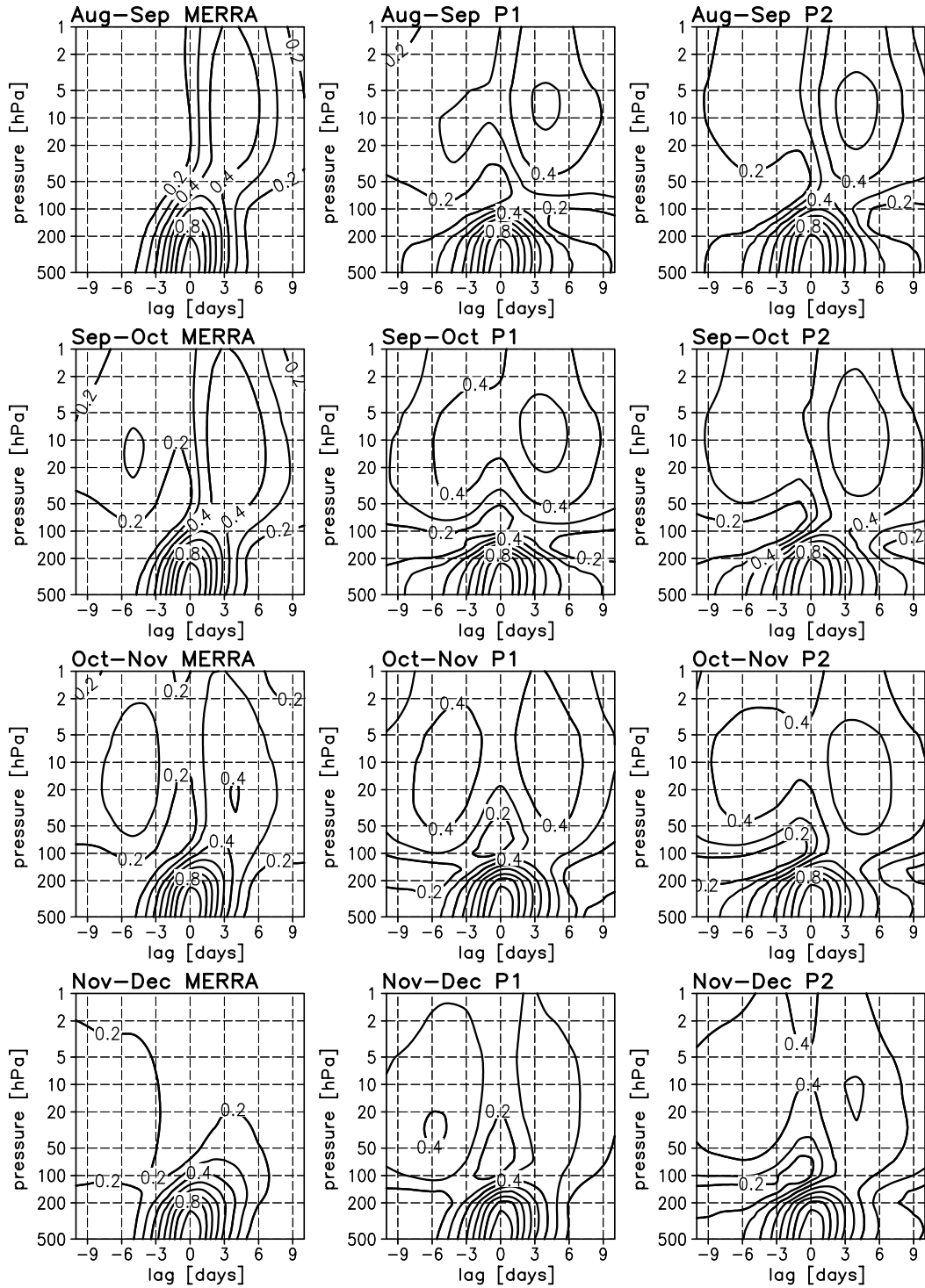


FIG. 1. Vertical-time lag section of the correlation coherence for wave-1 averaged from 45 to 80°S at 500 hPa with vertical levels between 500 and 1 hPa for two-month overlapping periods from August-September to November-December 1979 to 2004 and for time lags between -10 and 10 days. For negative time lags the stratosphere is leading the troposphere. The cross-correlations are shown for the MERRA data set (left column) and the P1 (middle column) and P2 (right column) GEOS CCM simulations. Only correlations which are statistically significant at the 99% levels are contoured and the contour interval is 0.1.

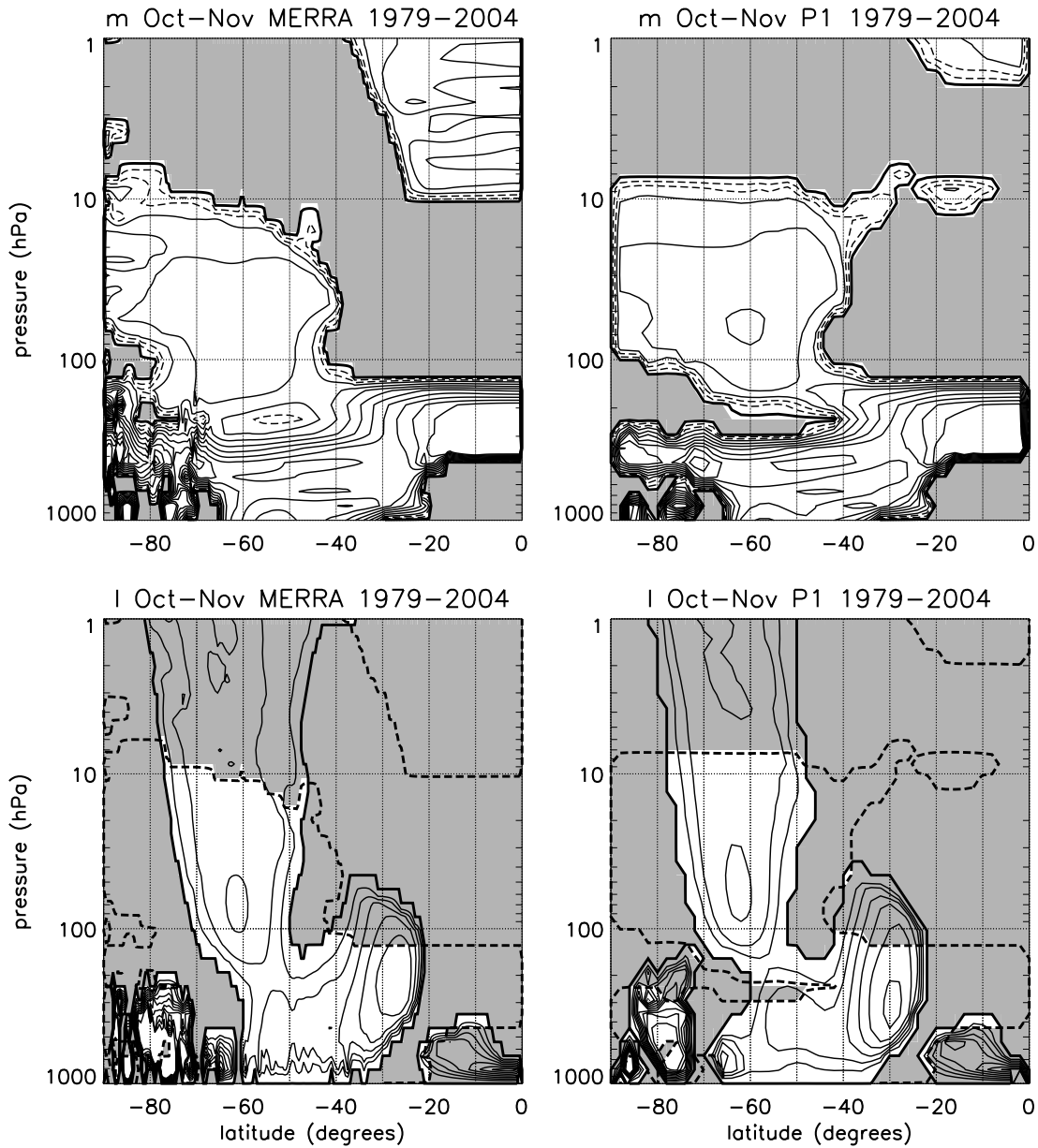


FIG. 2. Zonal-mean cross sections of the climatological vertical (top row) and meridional (bottom row) wavenumbers during October-November from 1979 to 2004 for the MERRA data set (left column) and the P1 GEOS CCM simulation (right column). For the vertical wavenumber the contours (units  $10^{-5} \text{ m}^{-1}$ ) are shown at 0.01 (thick line); 2, 4 (dashed line); 6-30 in jumps of 3 (thin lines) and the shading indicates regions of wave evanescence ( $m^2 < 0$ ). For the meridional wavenumber, the contour interval is  $1 \text{ rad}^{-1}$ , the thick line represents the 0.01 contour and the dashed line indicates the position of the vertical reflecting surface. Finally, the shading indicates regions of wave evanescence in the meridional ( $l^2 < 0$  bounded by solid line) and vertical ( $m^2 < 0$  bounded by dashed line) directions.

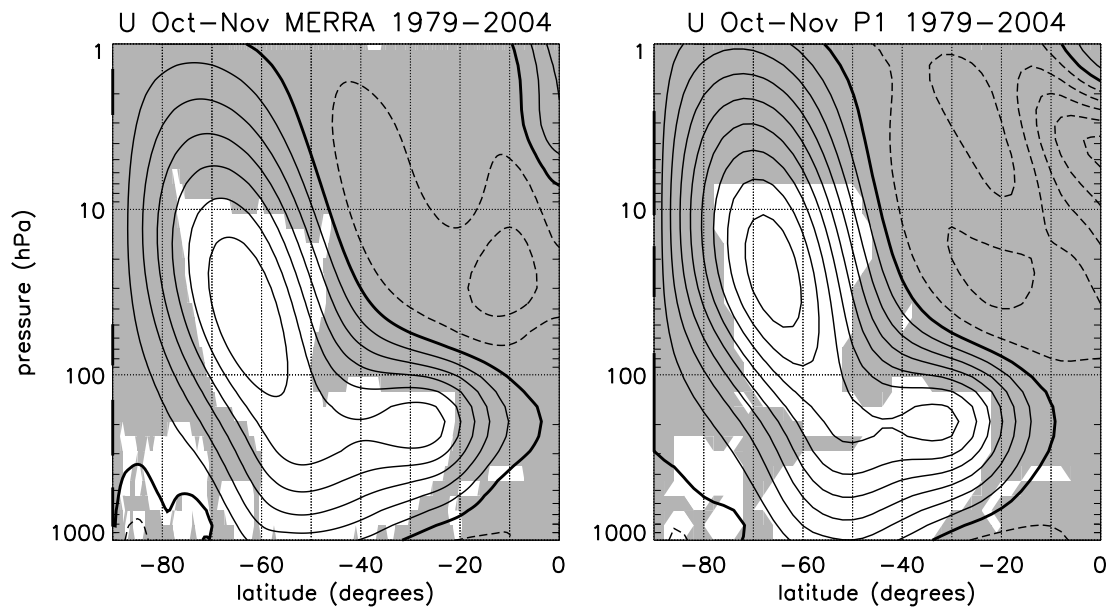


FIG. 3. Zonal-mean zonal wind during October-November from 1979 to 2004 for the MERRA data set (left panel) and the P1 GEOS CCM simulation (right panel). Contour interval is  $5 \text{ ms}^{-1}$  and negative contours are dashed. The thick line indicates the zero zonal-wind line and the shading represents regions of wave evanescence and is identical to the shaded regions in the lower panels of Fig. 2.

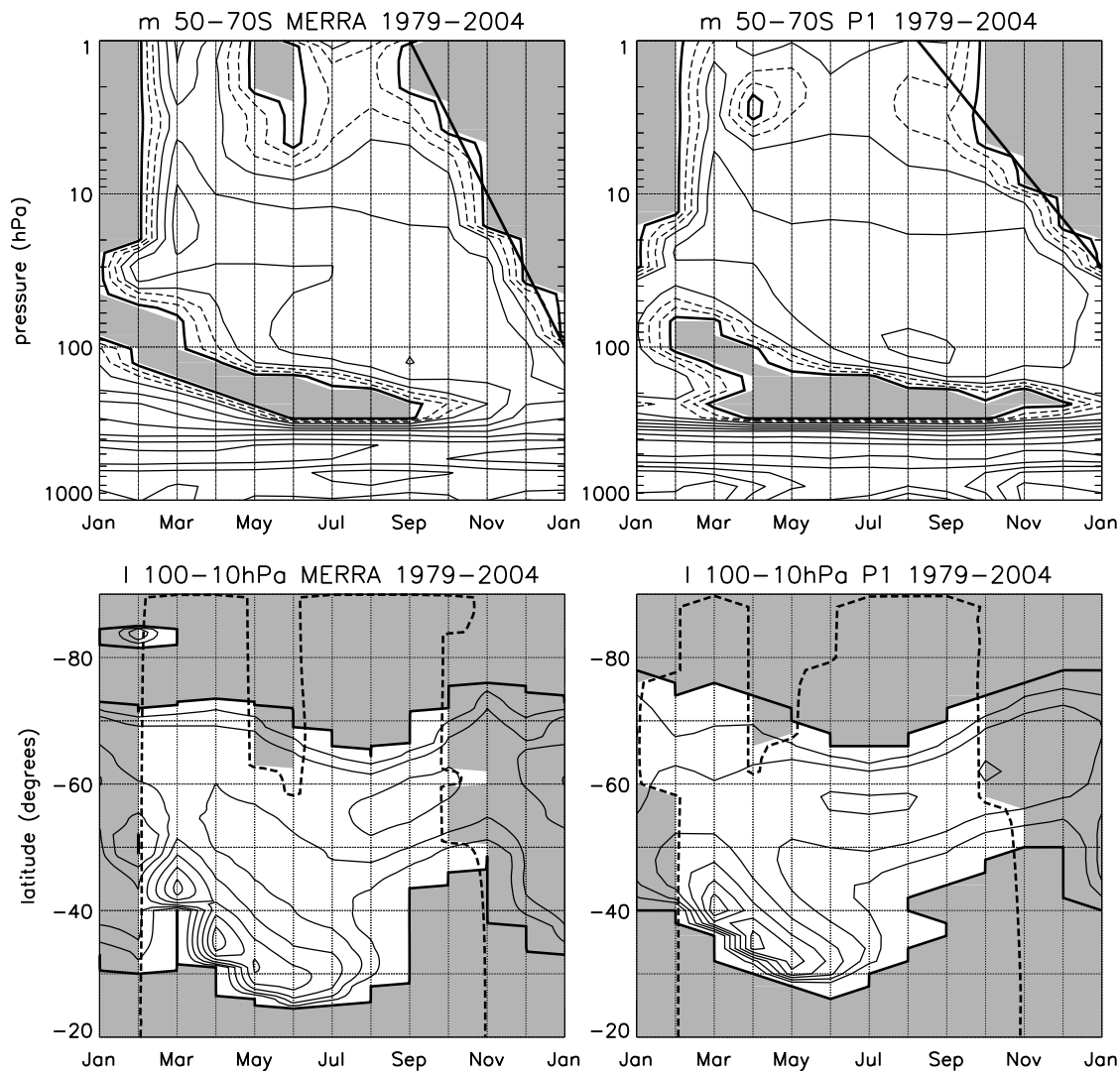


FIG. 4. The climatological seasonal cycle of the vertical (top row) and meridional (bottom row) wavenumbers averaged between 50 and 70°S and 100 and 10 hPa, respectively from 1979 to 2004 for the MERRA data set (left column) and the P1 GEOS CCM simulation (right column). Contouring and shading as in Fig. 2. The thick solid lines in the upper panels show the approximate linear descent rate. Overlying the climatological seasonal cycle of the meridional wavenumber is the seasonal cycle of the vertical wavenumber averaged between 3 and 1 hPa.

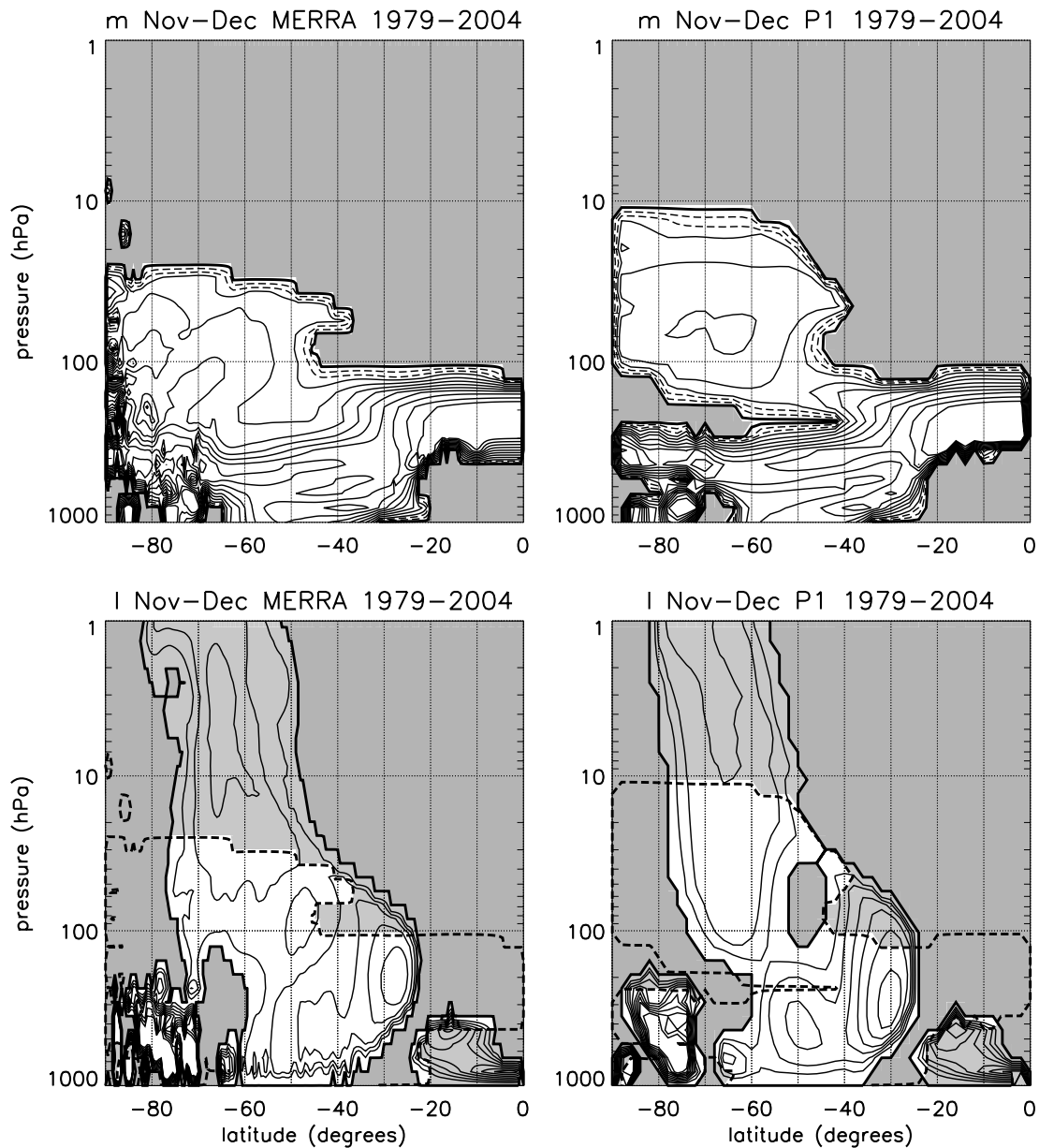


FIG. 5. Zonal-mean cross sections of the vertical (top row) and meridional (bottom row) wavenumbers during November–December from 1979 to 2004 for the MERRA data set (left column) and the P1 GEOS CCM simulation (right column). Contouring and shading as in Fig. 2.

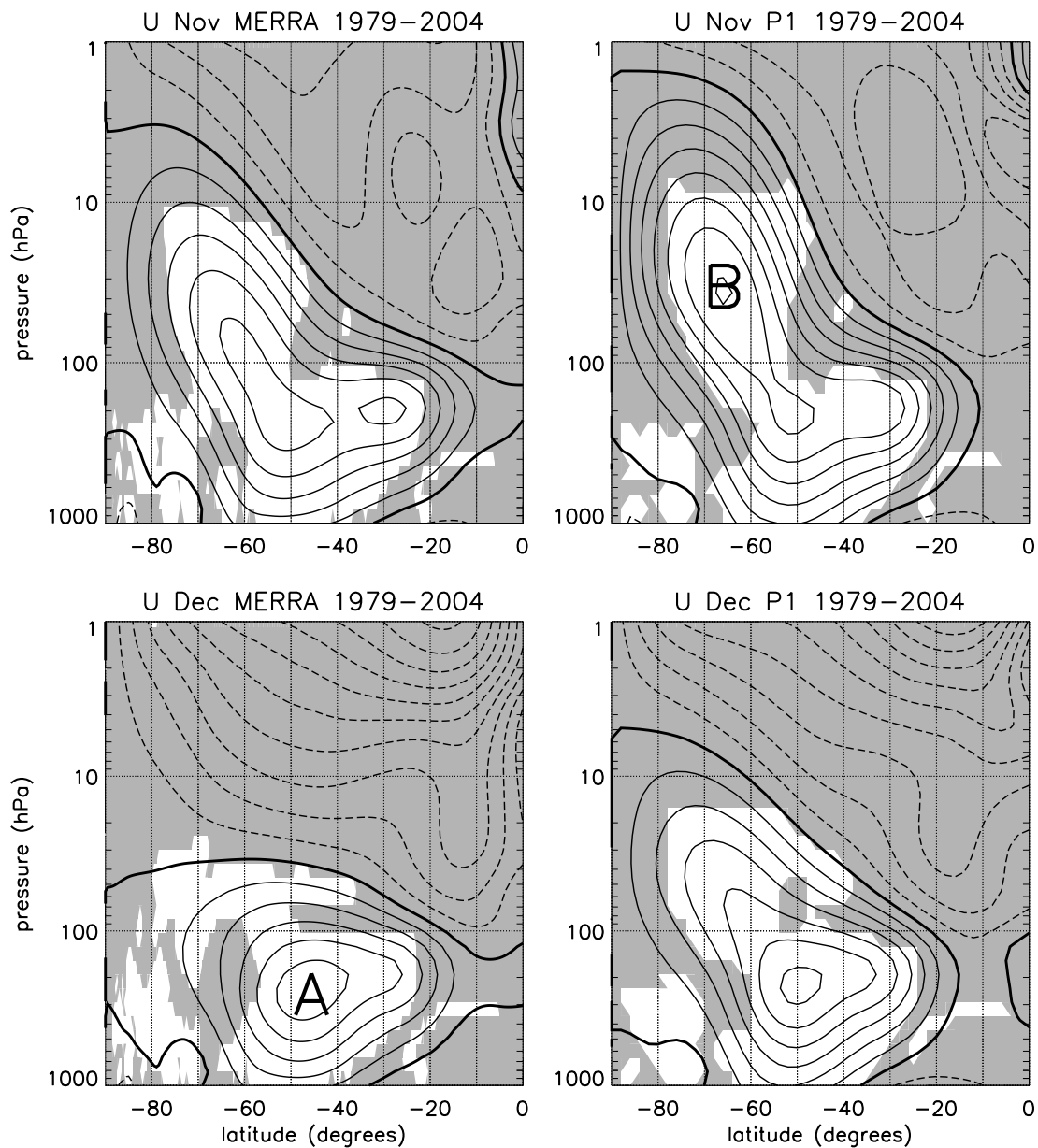


FIG. 6. Zonal-mean zonal wind during November (top row) and December (bottom row) from 1979 to 2004 for the MERRA data set (left column) and the P1 GEOS CCM simulation (right column). Contour interval is  $5 \text{ ms}^{-1}$  and negative contours are dashed. The thick line indicates the zero zonal-wind line and the shading represents regions of vertical and meridional wave evanescence. Letters A and B indicated regions discussed in the text.

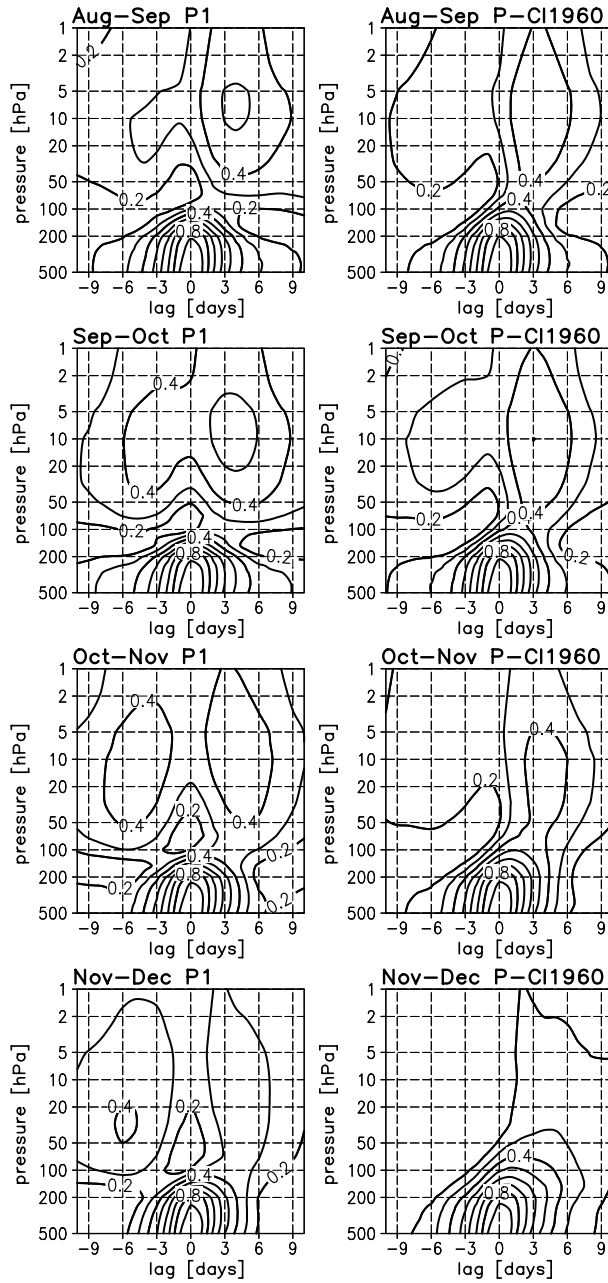


FIG. 7. Vertical-time lag section of the correlation coherence for wave-1 averaged from 45 to 80°S at 500 hPa with vertical levels between 500 and 1 hPa for two-month overlapping periods from August-September to November-December 1979 to 2004 and for time lags between -10 and 10 days. The cross-correlations are shown for the P1 (left column, repeated from Fig. 1) and the P-CI1960 (right column) GEOS CCM simulations. Contours and significance as in Fig. 1.

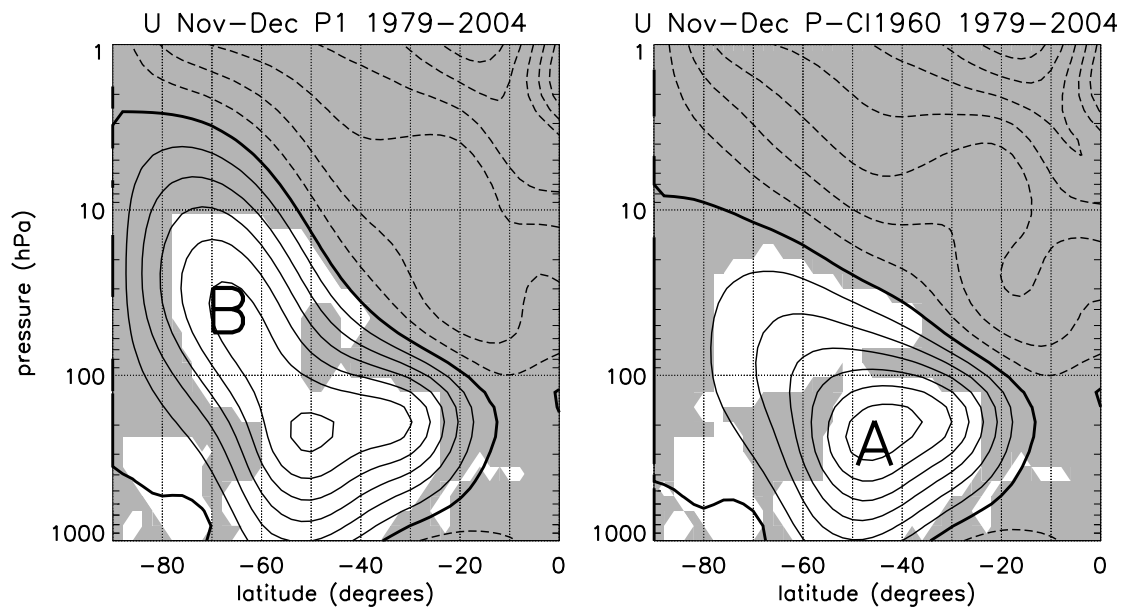


FIG. 8. Zonal-mean zonal wind during November-December from 1979 to 2004 for the P1 (left panel) and the P-CI1960 (right panel) GEOS CCM simulations. Contours and shading as in Fig. 3. Letters A and B indicated regions discussed in the text.

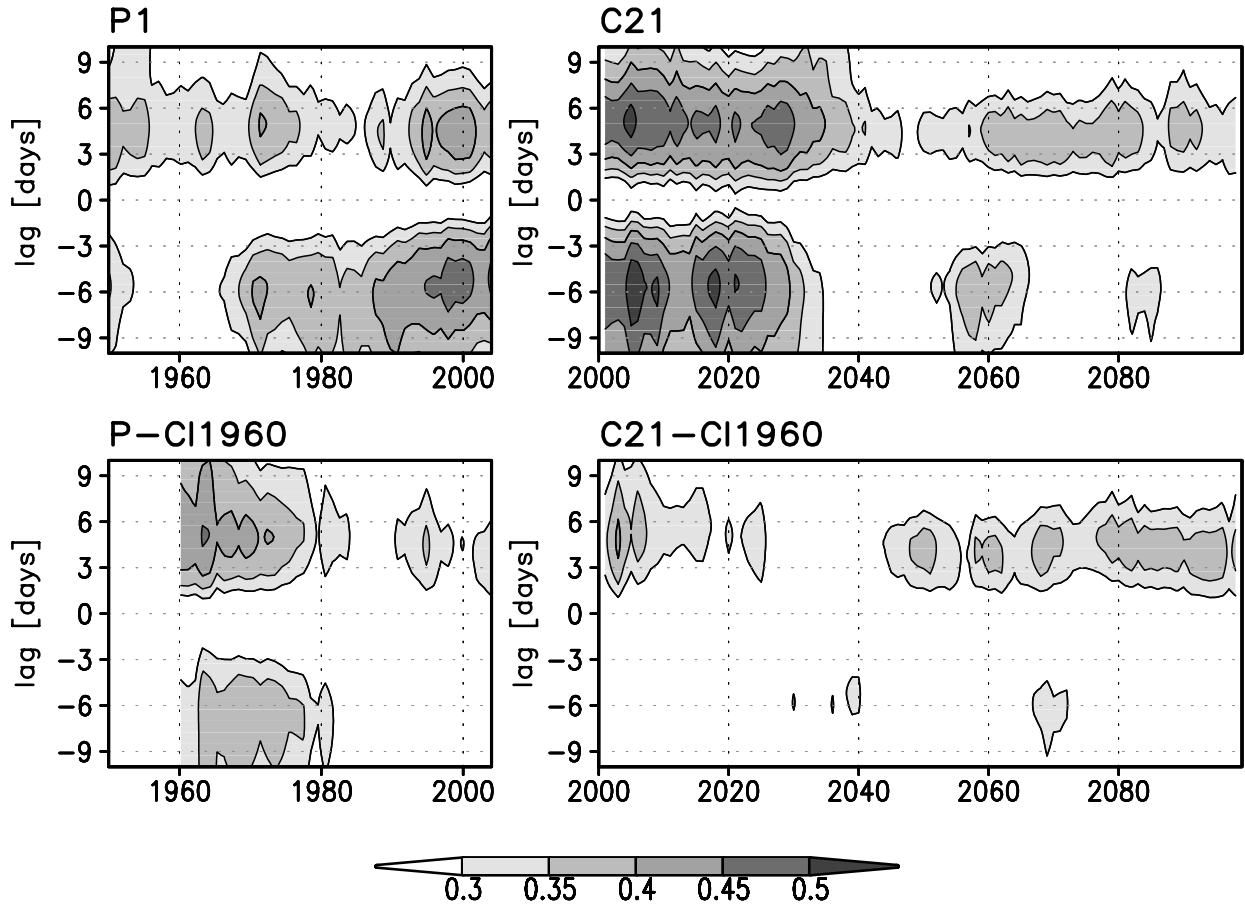


FIG. 9. Time series of the wave-1 cross-coherence correlations between 30 hPa and 500 hPa for wave-1 averaged from 45 to 80°S (solid lines) and for time lags between -10 and 10 days during November-December. The correlation time series are shown for the P1 (top left), C21 (top right), P-CI1960 (bottom left) and C21-CI1960 (bottom right) GEOS CCM simulations. The cross correlations were determined based on 15-year overlapping periods.

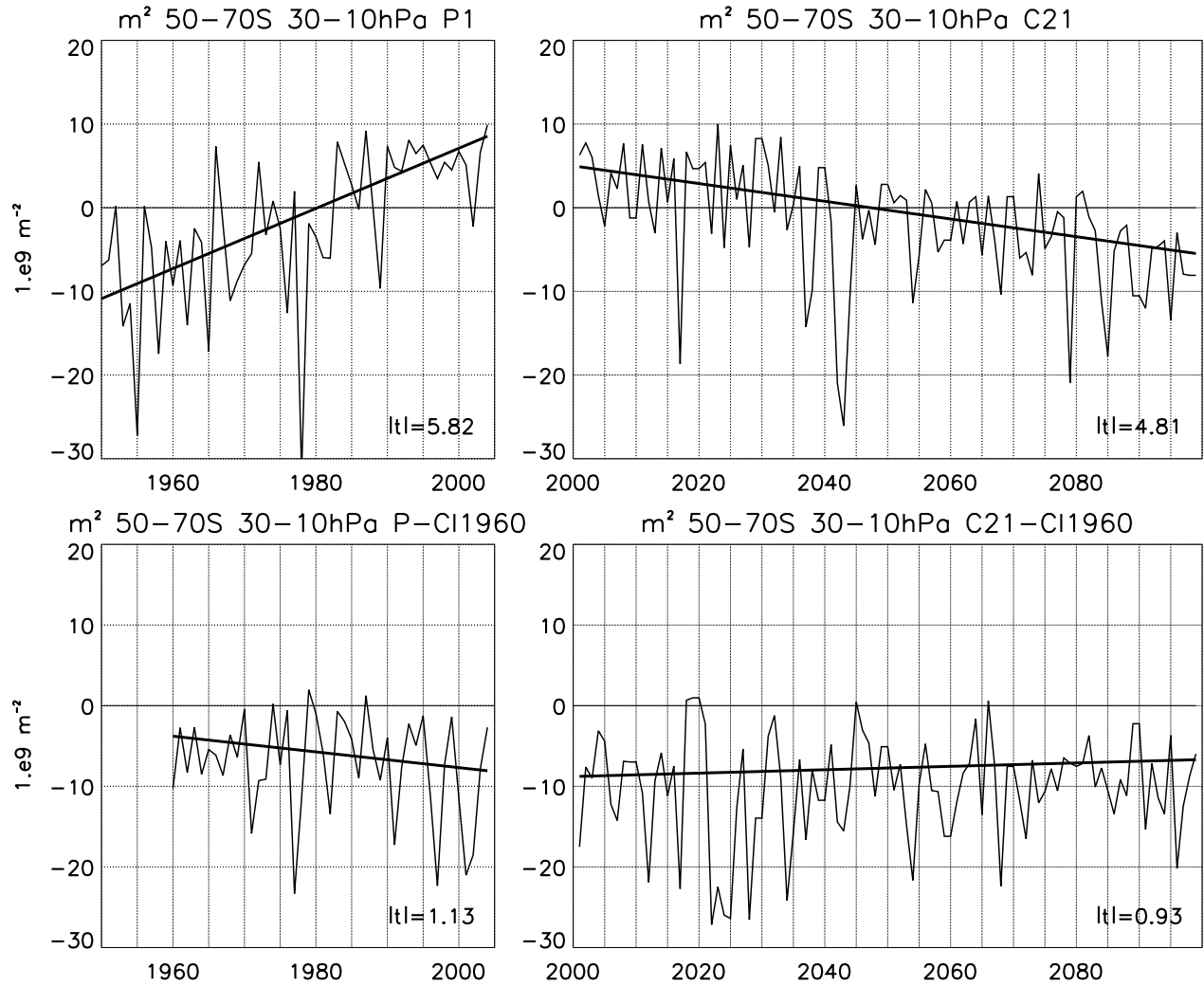


FIG. 10. Time series of the squared vertical wavenumber averaged between 50 and 70°S and 30 to 10 hPa for the P1 (top left), C21 (top right), P-CI1960 (bottom left) and C21-CI1960 (bottom right) GEOS CCM simulations. The thick solid line shows the linear regression and the associated t-value is shown at the bottom of each plot.

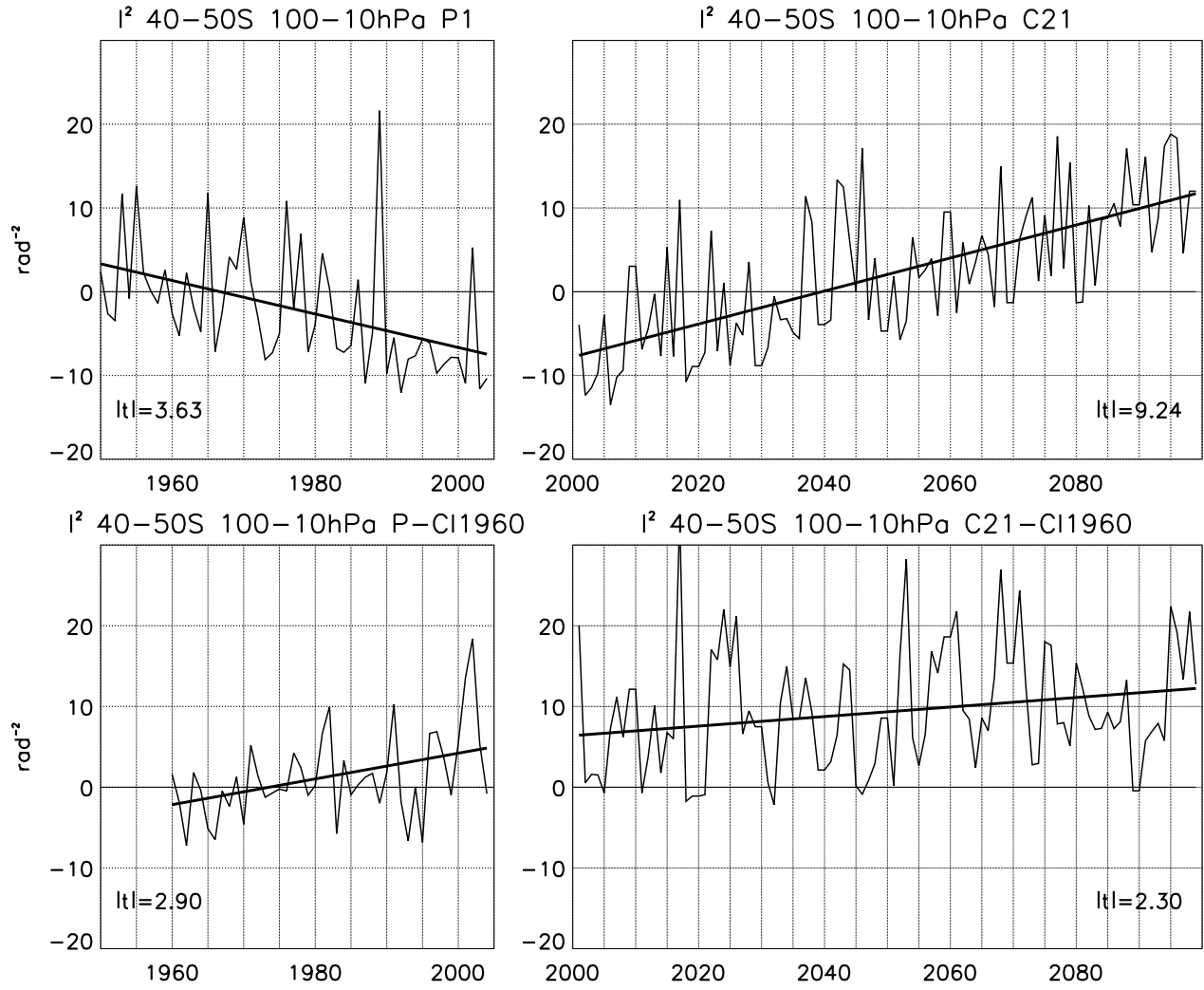


FIG. 11. Time series of the squared meridional wavenumber averaged between 40 and 50°S and 100 to 10 hPa for the P1 (top left), C21 (top right), P-CI1960 (bottom left) and C21-CI1960 (bottom right) GEOS CCM simulations. The thick solid straight line shows the linear regression and the associated t-value is shown at the bottom of each plot.

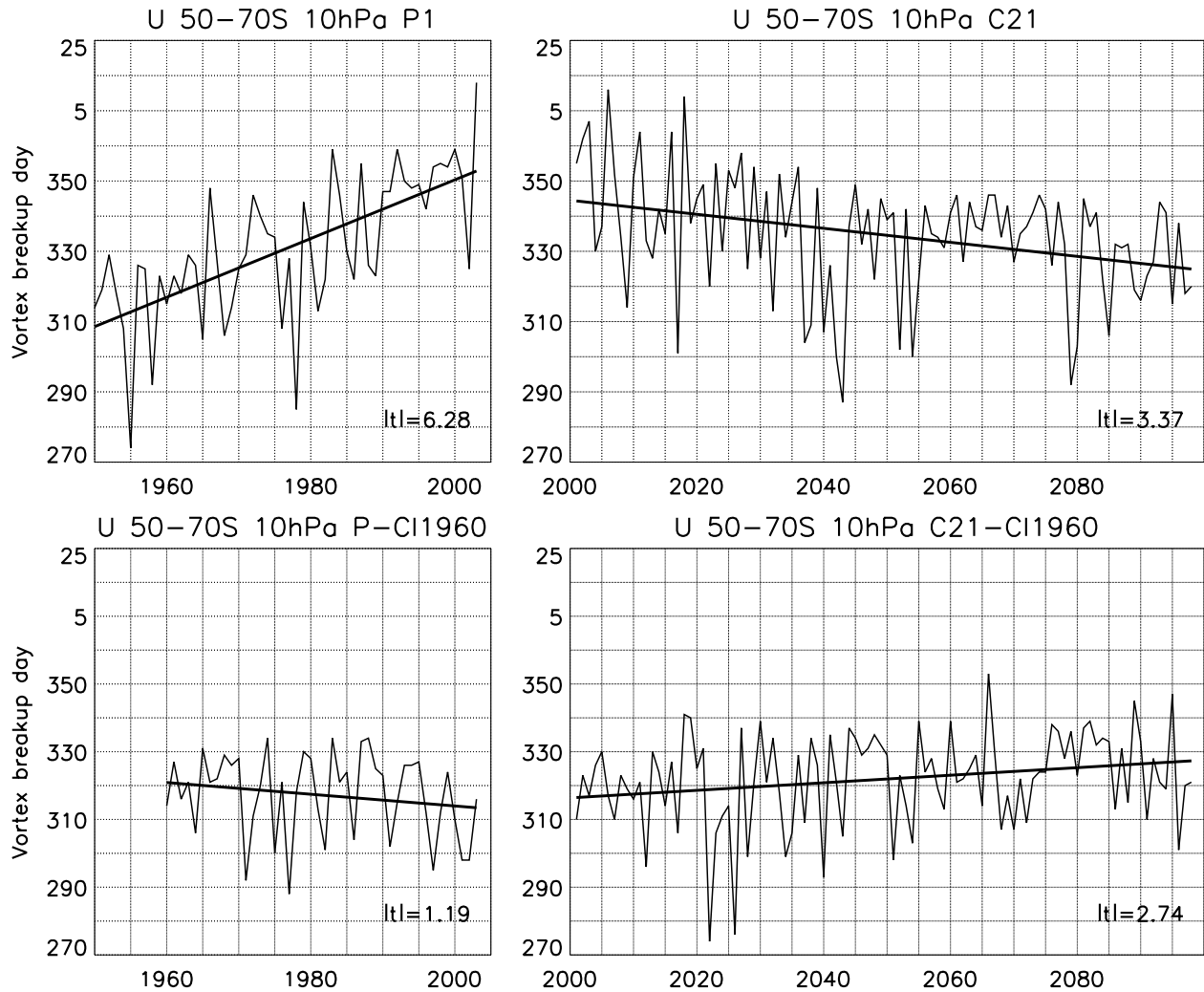


FIG. 12. Time series of the vortex breakup day, defined as the first day when the zonal-mean zonal wind averaged between 50 and 70°S at 10 hPa is negative, for the P1 (top left), C21 (top right), P-CI1960 (bottom left) and C21-CI1960 (bottom right) GEOS CCM simulations. The thick solid line shows the linear regression and the associated t-value is shown at the bottom of each plot.

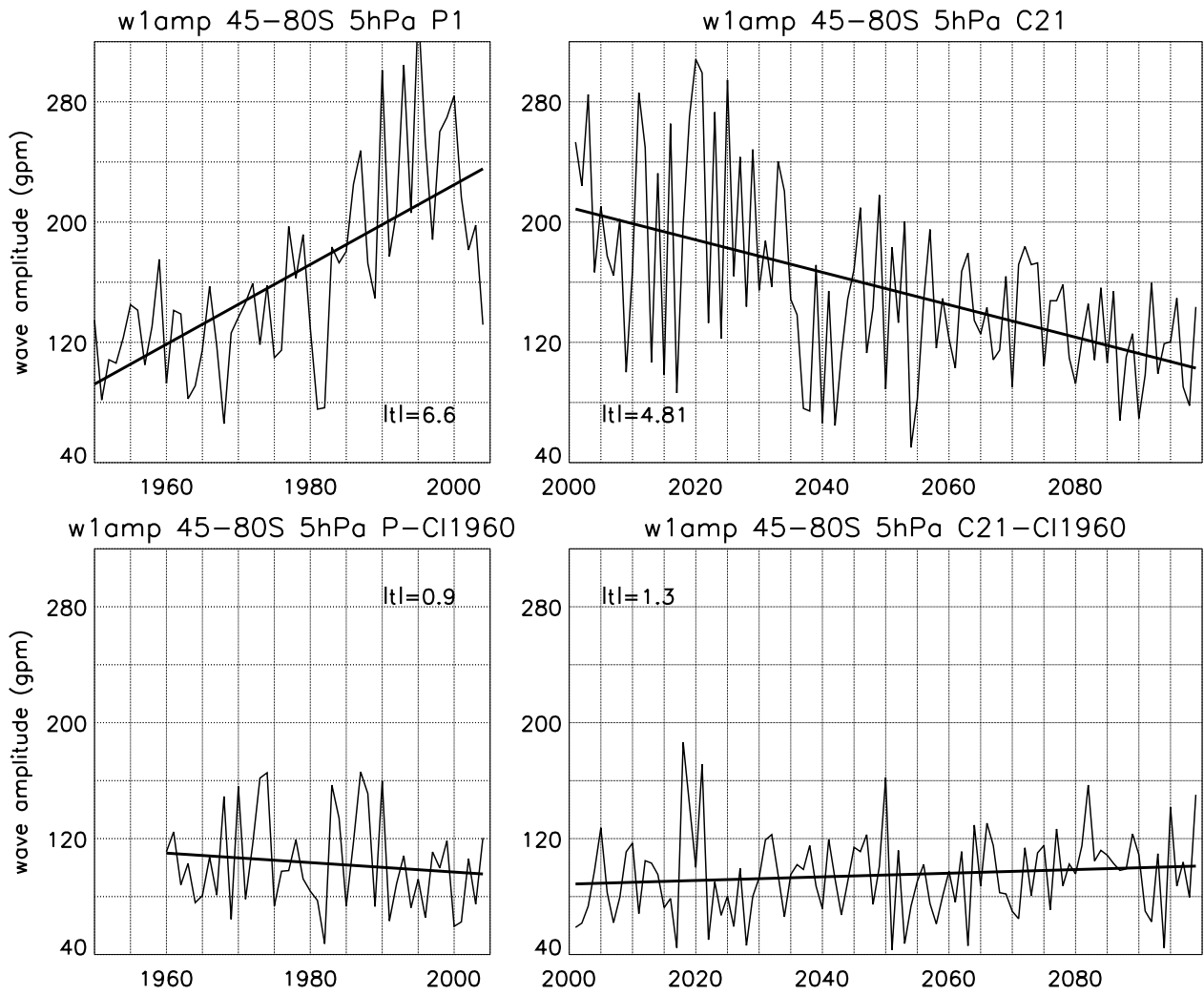


FIG. 13. Time series of wave-1 amplitude averaged between 45 and 80°S at 5 hPa for the P1 (top left), C21 (top right), P-CI1960 (bottom left) and C21-CI1960 (bottom right) GEOS CCM simulations. The thick solid line shows the linear regression and the associated t-value is also shown.

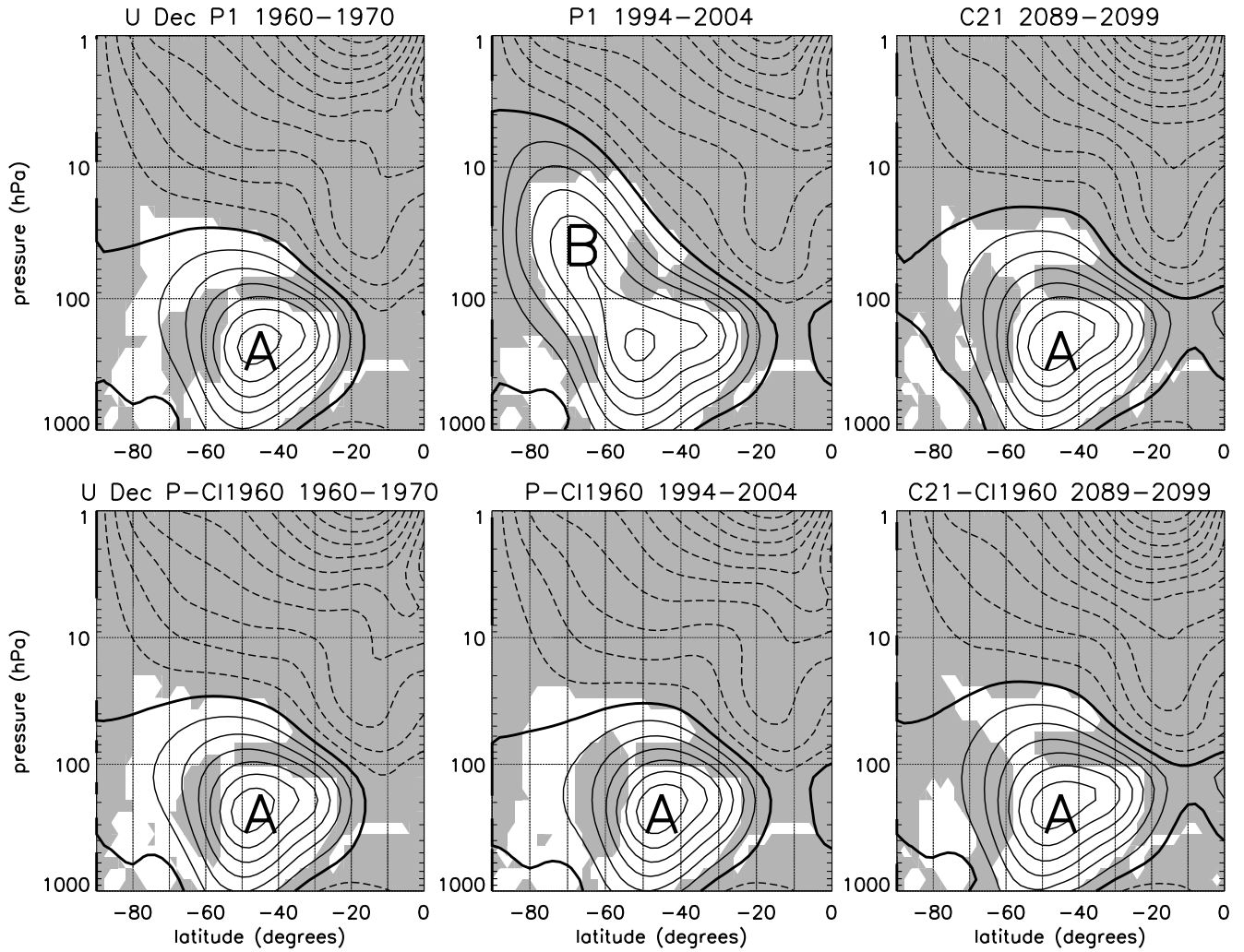


FIG. 14. Zonal-mean zonal wind and wave evanescence regions from the wave geometry (indicated by shading) from 1960 to 1970 (left column), 1994 to 2004 (middle column), and 2089 to 2099 (right column) during December for the P1 (top two left panels), C21 (top right panel), P-CI1960 (bottom two left panels) and C21-CI1960 (bottom right panel) GEOS CCM simulations. Contours as in Fig. 3. Letters A and B indicated regions discussed in the text.